Draft version 6 February 28, 2017
Preprint typeset using LaTeX style emulateapj v. 2/16/10

arXiv:1607.00688v2 [astro-ph.EP] 27 Feb 2017

HATS-22b, HATS-23b AND HATS-24b: THREE NEW TRANSITING SUPER-JUPITERS FROM THE HATSOUTH PROJECT†

J. Bento[1], B. Schmidt[1], J. D. Hartman[2], G. Á. Bakos[2], S. Ciceri[9,10], R. Brahm[3], D. Bayliss[5], N. Espinoza[3], G. Zhou[4], M. Rabus[3,9], W. Bhatti[2], K. Penev[2], Z. Csubry[2], A. Jordán[3,9], L. Mancini[9], T. Henning[9], M. de Val-Borro[2], C. G. Tinney[6,7], D. J. Wright[6,7], S. Durkan[11], V. Suc[3], R. Noyes[4], J. Lázár[8], I. Papp[8], P. Sári[8]

Draft version 6 February 28, 2017

ABSTRACT

We report the discovery of three moderately high-mass transiting hot Jupiters from the HATSouth survey: HATS-22b, HATS-23b and HATS-24b. These planets add to the number of known planets in the $\sim 2M_{\rm J}$ regime. HATS-22b is a $2.74 \pm 0.11\,M_{\rm J}$ mass and $0.953^{+0.048}_{-0.029}\,R_{\rm J}$ radius planet orbiting a $V = 13.455 \pm 0.040$ sub-solar mass ($M_\star = 0.759 \pm 0.019\,M_\odot$;$R_\star = 0.759 \pm 0.019\,R_\odot$) K-dwarf host star on an eccentric ($e = 0.079 \pm 0.026$) orbit. This planet's high planet-to-stellar mass ratio is further evidence that migration mechanisms for hot Jupiters may rely on exciting orbital eccentricities that bring the planets closer to their parent stars followed by tidal circularisation. HATS-23b is a $1.478 \pm 0.080\,M_{\rm J}$ mass and $1.69 \pm 0.24\,R_{\rm J}$ radius planet on a grazing orbit around a $V = 13.901 \pm 0.010$ G-dwarf with properties very similar to those of the Sun ($M_\star = 1.115 \pm 0.054$; $R_\star = 1.145 \pm 0.070$). HATS-24b orbits a moderately bright V=12.830 $\pm$ 0.010 F dwarf star ($M_\star = 1.218 \pm 0.036\,M_\odot$; $R_\star = 1.194^{+0.066}_{-0.041}\,R_\odot$). This planet has a mass of $2.39^{+0.21}_{-0.12}\,M_{\rm J}$ and an inflated radius of $1.516^{+0.085}_{-0.065}\,R_{\rm J}$.

Subject headings: planetary systems — stars: individual (HATS-22, GSC 6664-00373, HATS-23, GSC 8382-01464 HATS-24, GSC 9054-00129) techniques: spectroscopic, photometric

1. INTRODUCTION

Transiting planets are the key towards understanding the structure and composition of planetary systems. The breadth of system parameters that can be determined from the discovery data sets and follow-up studies surpasses any other detection method, the most important being the mass and radius, yielding an estimate of the bulk density. Moreover, these planets are amenable to transmission studies during transit (e.g. Bento et al. 2014; Jordán et al. 2013; Marley et al. 2013; Seager & Sasselov 2000; Pont et al. 2008; Sing et al. 2011), a direct measurement of the planet's day-side emission as an estimate of the surface temperature during secondary eclipse (Zhou et al. 2013, 2014; Knutson et al. 2008; Désert et al. 2011; Croll et al. 2011), and other properties (Louden & Wheatley 2015; Zhou et al. 2016; Collier Cameron et al. 2010; Hartman et al. 2015; Gandolfi et al. 2012).

In particular, the hundreds of hot Jupiters (broadly Jupiter mass planets orbiting close to their host stars on less that $\sim$ 10 day periods) found to date have challenged planetary formation theories and structure models. Despite an early suggestion of the possibility that such planets may exist by Struve (1952), explaining their existence is not trivial as they are not generally expected to form in-situ (Boss 1995; Lissauer 1995; Bodenheimer et al. 2000), with the migration potentially taking place in the very early early stages of formation (Donati et al. 2016). Recent work suggests that there is a potential mechanism that can form such planets in-situ (Batygin et al. 2016), but the general consensus is that these planets are formed at large separations and migrate inwards to their current positions, and several possible mechanisms have been suggested for this process. A disk migration scenario has been proposed in

[1] Research School of Astronomy and Astrophysics, Mount Stromlo Observatory, Australian National University, Cotter Road, Weston, ACT 2611, Australia. joao.bento@anu.edu.au
[2] Department of Astrophysical Sciences, 4 Ivy Ln., Princeton, NJ 08544
[3] Instituto de Astrofísica, Facultad de Física, Pontificia Universidad Católica de Chile, Av. Vicuña Mackenna 4860, 7820436 Macul, Santiago, Chile
[4] Harvard-Smithsonian Center for Astrophysics, Cambridge, MA 02138, USA
[5] Observatoire Astronomique de l'Université de Genéve, 51 ch. des Maillettes, 1290 Versoix, Switzerland
[6] Australian Centre for Astrobiology, School of Physics, University of New South Wales, NSW 2052, Australia
[7] Exoplanetary Science at UNSW, School of Physics, University of New South Wales, NSW 2052, Australia
[8] Hungarian Astronomical Association, Budapest, Hungary
[9] Max Plank Institute for Astronomy, Königstuhl 17, 69117 Heidelberg, Germany
[10] Department of Astronomy, Stockholm University, SE-106 91 Stockholm, Sweden
[11] Astrophysics Research Centre, School of Mathematics & Physics, Queen's University, Belfast BT7 1NN, UK

† The HATSouth network is operated by a collaboration consisting of Princeton University (PU), the Max Planck Institute für Astronomie (MPIA), the Australian National University (ANU), and the Pontificia Universidad Católica de Chile (PUC). The station at Las Campanas Observatory (LCO) of the Carnegie Institute is operated by PU in conjunction with PUC, the station at the High Energy Spectroscopic Survey (H.E.S.S.) site is operated in conjunction with MPIA, and the station at Siding Spring Observatory (SSO) is operated jointly with ANU. Based in part on data collected at Subaru Telescope, which is operated by the National Astronomical Observatory of Japan. Based in part on observations made with the MPG 2.2 m Telescope at the ESO Observatory in La Silla.

which the orbiting planet exchanges angular momentum with the protoplanetary disk and loses orbital momentum, thereby starting out at large separations and making its way in to close to the host star (e.g. Alibert et al. 2005; Chambers 2009; Rice et al. 2008, and references therein). Alternatively, interactions with other bodies in the system can cause scattering/ejection events and the planet in question is forced into an eccentric orbit that brings it closer to the host star (e.g. Rasio & Ford 1996; Ford & Rasio 2008). Tidal interactions are then thought to circularise the orbit resulting in close-in planets. Other processes suggested include Kozai migration, first proposed by Wu & Murray (2003), which states that a highly inclined stellar companion can induce Kozai oscillations (Kozai 1962) in the planet and excite it to progressively higher eccentricity. We note, however, that Ngo et al. (2016) suggest that only a small fraction (<20%) of hot Jupiter host stars have stellar companions capable of inducing such oscillations. Very recent works by Petrovich (2015) and Wu & Lithwick (2011) suggest that *secular migrations* may occur due to interactions between two-or-more well-spaced, eccentric planets, which can cause one of them to become very eccentric on long timescales, leading to both enhanced eccentricity and tidal dissipation over larger timescales (Lithwick & Wu 2011). However, recent results show that an understanding of planet formation and migration has not been achieved yet. Antonini et al. (2016) suggest that perhaps hot Jupiters with outer companions are unlikely to have migrated through high-eccentricity processes due to the instability of their orbits, while Schlaufman & Winn (2016) find that warm Jupiters are no more likely to have wide orbit planetary companions than those in longer orbits, which is at odds with an eccentric migration scenario.

The possibility that there is a mass dependence in the question of planet migration and eccentricity is supported by evidence that higher mass planets tend to show higher eccentricity than those less massive than $2M_{\rm J}$ (Mazeh et al. 1997; Marcy et al. 2005; Southworth et al. 2009). Moreover, it seems that planets at higher orbital separation/period also have a higher tendency to show non-zero eccentricities (Pont et al. 2011) versus close-in planets. This raises questions such as: are high-mass planets more susceptible to retain large eccentricities on longer timescales? And, if so, is this an indication that planet-planet scattering, predicted to generate high eccentric orbits, is likely to be the main migration mechanism for planetary systems? Is the structure and evolution of high and low-mass planets fundamentally different? Are hot Jupiter structures fundamentally affected by extreme cases of inwards migration and current irradiation levels? The answer lies on a larger sample and better understanding of the composition of these planets.

In this paper we report the discovery of three new transiting super Jupiters with masses higher than $1.4M_{\rm J}$ from the HATSouth survey: HATS-22b, HATS-23b and HATS-24b. These planets add to the list of of well-characterised massive hot Jupiters which collectively pose a challenge to models of planetary formation and migration.

In Section 2 we describe the photometric and spectroscopic observations undertaken for all three targets in the pursuit of determining their planetary nature. Section 3 contains a description of the global data analysis and presents the modelled stellar and planetary parameters. We also describe the methods employed to reject false positive scenarios. Our findings are finally discussed in Section 4.

2. OBSERVATIONS

Periodic planetary transit-like signals in any time-series photometric survey can be created by a range of astrophysical events which include grazing binary stellar eclipses, transits by planet-sized dwarf stars and eclipsing binary systems whose light is blended with a nearby foreground or background star. As such, a substantial follow-up campaign is required using both photometric and spectroscopic observations. In this section we describe the full set of observations that led to the detection and confirmation of the planets presented in this paper.

2.1. *Photometric detection*

The HATSouth project is a collaboration between Princeton, the Australian National University, The Max Plank Institute for Astronomy, and the Pontificia Universidad Católica de Chile, dedicated to finding transiting planets hosted by bright stars in the southern hemisphere (Bakos et al. 2013). It is the largest ground-based search for transiting extrasolar planets in the world, with a three-site network (Las Campanas Observatory in Chile, the High Energy Spectroscopic Survey (H.E.S.S.) site in Namibia and Siding Spring Observatory, Australia) capable of continuously monitoring 128 sq degree fields in the southern hemisphere. The project has commissioned six enclosures, two per site, each containing four telescopes on a single mount. Discoveries include the notable case of HATS-17b (Brahm et al. 2016b), which is the largest period transiting exoplanet found to date from a ground-based survey, thereby demonstrating HATSouth's unique strength in its longitude coverage. A full list of discovered planets along with discovery light curves can be found at http://hatsouth.org/

Table 1 shows a summary of the photometric observations for the planetary systems HATS-22, HATS-23 and HATS-24. For HATSouth data we list the HATSouth unit, CCD and field name from which the observations were taken. The detection of all targets relied on data from all HATSouth telescopes, HS-1 and HS-2 located in Chile, HS-3 and HS-4 in Namibia and HS-5 and HS-6 in Australia. The data gathered at different time periods between 2011/04 and 2013/11 for different targets, as described in Table 1, resulted in a total of 13,129 data points for HATS-22, 22,937 observations of HATS-23 and 4,406 points for HATS-24.

All HATSouth observations are obtained through a Sloan r filter with a typical exposure time of 240 seconds. The data were reduced with the custom pipeline described by Penev et al. (2013) and the light curves were detrended using an External Parameter Decorrelation method (Bakos et al. 2013) followed by the application of the Trend Filtering Algorithm (TFA, Kovács et al. 2005). A Box Least-Squares algorithm (BLS; see Kovács et al. 2002) was then used to search for periodic transit-like signals. The resulting discovery light curves phase-folded to the highest likelihood periods are shown in Figure 1.

After having removed the best fit Box Least Squares model corresponding to the hot-Jupiter transit signal from the light curves, we searched for additional periodic signals with the aim to detect potential stellar activity or other transiting planets in each of the three systems. The light curves for all targets did not reveal any other significant signals, defined as those with a formal false alarm probability, assuming Gaussian white noise, of less than 0.1%, on a second BLS pass of the residuals. We therefore find no evidence for additional transiting planets in the systems. However, a Generalised Lomb Scargle (GLS, Zechmeister & Kürster 2009) routine, looking for sinusoidal patterns that can be related to activity, revealed a significant peak at a period of 7.49 ± 0.25 days for HATS-23 with a false alarm probability of 10^{-21}. This is shown in Figure 2 (left-hand panel). Further inspection of this signal reveals a sinusoidal signal (right-hand panel) that can be attributed to activity such as stellar spots on the surface of the host star modulating the light curve. We note that the detected 7.49 day period is not consistent with the stellar rotation period estimated from $v \sin i$ (13.1 ± 1.4 days) assuming an aligned stellar rotation axis. If the detected sinusoidal signal is indeed real and related to the stellar rotation, this may suggest a moderately high misalignment between the orbital plane and the stellar rotational axis. On the other hand, we can not definitively exclude the possibility that the true rotation period is double this value, which would be consistent with the observed $v \sin i$. However, when the light curve is folded at twice the 7.49 day period it reveals a double oscillation and the power of the window function at this period is substantially lower. Nevertheless, more observations of this system are required to address this dichotomy.

2.2. *Spectroscopic Observations*

2.2.1. *Reconnaissance spectroscopic observations*

The initial follow-up phase for all HATSouth planet candidates is carried out with reconnaissance spectra taken with the WiFeS instrument on the 2.3m ANU telescope at Siding Spring Observatory (SSO) (Dopita et al. 2007). Observations at $R \equiv \Delta\lambda/\lambda \approx 3000$ were taken to determine the stellar type of the host star, using the blue arm of the spectrograph. We estimate three key stellar properties, the effective temperature $T_{\rm eff}$, $\log g_\star$ and [Fe/H], by performing a grid search minimizing the χ^2 between the observed normalised spectrum and synthetic templates from the MARCS model atmospheres (Gustafsson et al. 2008). 2MASS J-K colors are used to restrict the $T_{\rm eff}$ parameter space and extinction correction is applied using the method of Cardelli et al. (1989). A detailed description of the observing and data reduction procedure is described in Bayliss et al. (2013). This type of observation is performed to identify giant host stars, for which the observed dip in its light curve could only have been caused by a stellar companion, and to identify stars not suitable for precise radial velocity follow-up due to high $T_{\rm eff}$ or high $v \sin i$. In addition, observations are taken at predicted quadrature phase with WiFeS using a mid-resolution $R \sim 7,000$ grating to perform radial velocity measurements at a precision of $\sim 2 \mathrm{km\,s^{-1}}$. We use a cross-correlation method against RV standards observed every night, using bracketed Ne-Ar exposures and a selection of telluric lines for calibration. This is, however, dependent on stellar type and signal-to-noise of each individual target. This allows for the detection of radial velocity variations above $\sim 5 \mathrm{km\,s^{-1}}$, and the exclusion of any targets showing large variations indicating that the transiting companion is a star. Details of these observations can be found in Table 2 and are described here:

- For HATS-22 we found an effective temperature of $4600 \pm 300K$, $\log g_\star$ of 4.8 ± 0.3 dex and metallicity of [Fe/H] $= -0.5 \pm 0.5$ dex, leading to the conclusion that this is a K-dwarf host star. Two measurements showed no clear variation at quadrature.
- For HATS-23 we found an effective temperature estimate of $5900 \pm 300K$, $\log g_\star$ of 4.5 ± 0.3 dex and metallicity of [Fe/H] $= 0.0 \pm 0.5$ dex. We conclude that the host star is of F or G-type. A single radial velocity measurement with WiFeS was taken but later complemented by observations with the FEROS spectrograph (see Section 2.2.2).
- HATS-24 was found to have an effective temperature of $5800 \pm 300K$, $\log g_\star$ of 3.4 ± 0.3 dex and metallicity of [Fe/H] $= -0.5 \pm 0.5$ dex. Based on this we concluded that the target is a G or F star, but the surface gravity suggested that this is a subgiant. Three radial velocity measurements taken showed no significant variation in the covered orbital phase.

Having excluded clear eclipsing binaries and giant host stars, these targets were then promoted to the next steps in the follow-up campaign, leading to further higher radial velocity precision spectroscopy and photometric follow-up.

2.2.2. *High-precision spectroscopic observations*

A full radial velocity characterisation covering a wide portion of the orbital phase of all of our targets is required in order to determine fundamental parameters such as mass and eccentricity of the orbits. Observations with the High Accuracy Radial Velocity Planet Searcher (Mayor et al. 2003, HARPS), fed by the ESO 3.6m telescope at $R \sim 115,000$ were obtained for HATS-22 and HATS-24, as well as $R \sim 60,000$ spectra using the CORALIE spectrograph (Queloz et al. 2001) fed by the 1.2m Euler telescope, both located at La Silla Observatory (LSO), Chile. All three targets were also monitored for radial velocity measurements using the FEROS spectrograph (Kaufer & Pasquini 1998, $R \sim 48,000$) fed by the MPG 2.2m telescope at LSO. The data reduction for all these spectra was performed using the method described in Jordán et al. (2014), with modifications to accommodate the different formats of the FEROS and HARPS data. Additionally, eleven spectra of HATS-24 were also obtained at $R \sim 70,000$ with the CYCLOPS2 fibre-feed and the UCLES spectrograph on the 3.9m Anglo-Australian telescope (AAT) at SSO and the data were reduced using the methods described in Addison et al. (2013). Further details about these observations can be found in Table 2. The resulting data sets for all targets can be found in Table 6 at the end of the

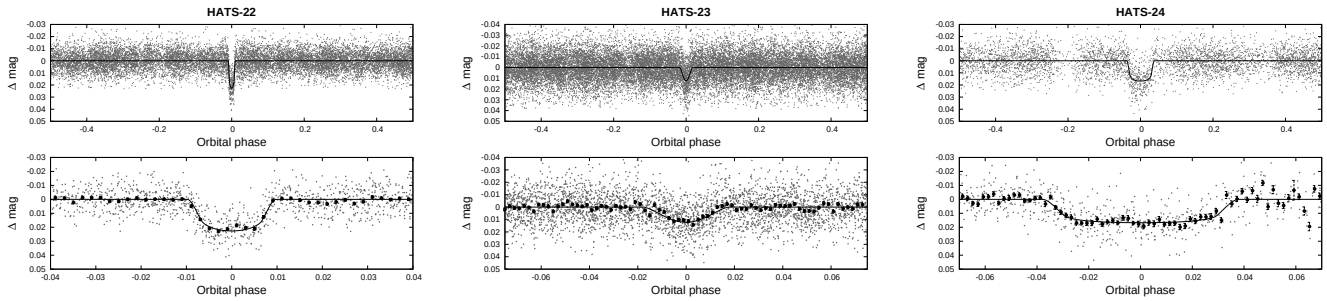

Figure 1. Phase-folded unbinned HATSouth light curves for HATS-22 (left), HATS-23 (middle) and HATS-24 (right). In each case we show two panels. The top panel shows the full light curve, while the bottom panel shows the light curve zoomed-in on the transit. The solid lines show the model fits to the light curves. The dark filled circles in the bottom panels show the light curves binned in phase with a bin size of 0.002.

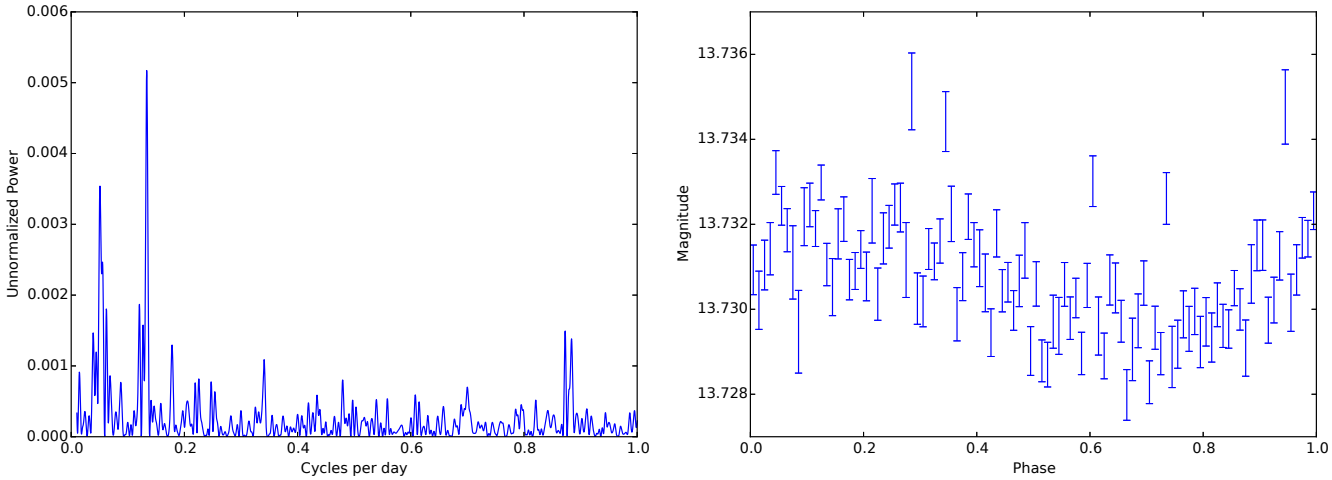

Figure 2. Additional period detected on the discovery light curve of HATS-23b. *Left:* We show the Lomb-Scargle periodogram produced using the method of Zechmeister & Kürster (2009) after removal of the transit signal. *Right:* The phase folded lightcurve on the 7.4965 day period equivalent to the highest peak binned in 0.01 phase intervals. The error bars shown are calculated through post binning error propagation of the original magnitude errors of individual measurements.

paper, and are shown in Figure 3, which includes radial velocity curves, best-fit models and bisector span (BS) estimates shown in the bottom panels for each target. All systems clearly show a radial velocity variation consistent with the detected orbital period from the photometric light curves and no clear correlation between the radial velocity measurements and the bisector-spans, indicating the systems are likely bona fide transiting planets (see Section 3.2).

2.3. *Photometric follow-up observations*

The three candidates were all photometrically followed-up employing the Las Cumbres Observatory Global Network of telescopes (Brown et al. 2013), specifically using the 1m sized telescopes of this network. These observations are undertaken to confirm the transit signal as well as refine the derived transit parameters from the HATSouth photometry. A single full transit of HATS-22 was observed in March 2015 using the i-band filter in which 85 images at a 226 second cadence were obtained. A single transit of HATS-24 in June of the same year was also obtained, consisting of 90 images with 151 second cadence. Due to the grazing nature of HATS-23 a larger number of photometric follow-up observations were required. Two full and two partial transits of HATS-23 were observed between July and September 2015 (inclusive), the first three in the i-band and the last using the z-band filter. The light curves for these high-precision photometric observations are shown in Figure 4 along with the best-fit models. The photometric data were taken and reduced using the same strategy and methods described in Penev et al. (2013), with details of setup in Bayliss et al. (2015), using a customisable pipeline. This pipeline uses standard photometric reduction frames (master bias, darks, twilight flats) and the DAOPHOT aperture photometry package for flux extraction of target and comparison stars. A quadratic trend in time as well as variations correlated with PSF shape were fitted simultaneously with the transit shape to compensate for differential refraction effects due to airmass and poor seeing. The *"V"-shaped* transit signal for HATS-23 is clearly indicative of the grazing nature of the planetary system and the consistent depth of the transits in both observed bands for this target also suggests that this is not an eclipsing binary system or a hierarchical triple system. The data from all photometric follow-up are available in electronic format in Table 3 and all photometric follow-up observations are also summarized in Table 1.

Table 1
Summary of photometric observations

Instrument/Field[a]	Date(s)	# Images	Cadence[b] (sec)	Filter	Precision[c] (mmag)
HATS-22					
HS-2.2/G610	2011 Apr–2013 Jul	5368	280	r	7.9
HS-4.2/G610	2013 Jan–2013 Jul	3755	289	r	7.2
HS-6.2/G610	2011 Apr–2013 Jul	4006	282	r	7.6
LCOGT 1 m+CTIO/sinistro	2015 Mar 30	85	226	i	1.0
HATS-23					
HS-1.2/G747	2013 Mar–2013 Oct	4233	287	r	12.6
HS-2.2/G747	2013 Sep–2013 Oct	648	287	r	12.3
HS-3.2/G747	2013 Apr–2013 Nov	9020	297	r	12.1
HS-4.2/G747	2013 Sep–2013 Nov	1460	297	r	13.6
HS-5.2/G747	2013 Mar–2013 Nov	6013	297	r	11.9
HS-6.2/G747	2013 Sep–2013 Nov	1563	290	r	14.9
LCOGT 1 m+SSO/SBIG	2015 Jul 07	22	194	i	2.1
Swope 1 m/e2v [d]	2015 Jul 15	51	139	i	13.7
LCOGT 1 m+SSO/SBIG	2015 Aug 30	34	192	i	3.1
LCOGT 1 m+CTIO/sinistro	2015 Sep 05	47	223	i	1.2
LCOGT 1 m+SAAO/SBIG	2015 Sep 16	39	201	z	4.8
HATS-24					
HS-1.1/G777	2011 May–2012 Sep	1513	298	r	9.1
HS-3.1/G777	2011 Jul–2012 Sep	1688	297	r	9.4
HS-5.1/G777	2011 May–2012 Sep	1205	296	r	9.3
LCOGT 1 m+SAAO/SBIG	2015 Jun 07	90	151	i	1.6

[a] For HATSouth data we list the HATSouth unit, CCD and field name from which the observations are taken. HS-1 and -2 are located at Las Campanas Observatory in Chile, HS-3 and -4 are located at the H.E.S.S. site in Namibia, and HS-5 and -6 are located at Siding Spring Observatory in Australia. Each unit has 4 CCDs. Each field corresponds to one of 838 fixed pointings used to cover the full 4π celestial sphere. All data from a given HATSouth field and CCD number are reduced together, while detrending through External Parameter Decorrelation (EPD) is done independently for each unique unit+CCD+field combination.
[b] The median time between consecutive images rounded to the nearest second. Due to factors such as weather, the day–night cycle, guiding and focus corrections the cadence is only approximately uniform over short timescales.
[c] The RMS of the residuals from the best-fit model.
[d] The Swope 1 m observations of HATS-23 produced very poor quality photometry due to adverse weather conditions, so we excluded them from the analysis of this system.

2.4. *Lucky imaging observations*

High spatial resolution "lucky" imaging observations were made of HATS-22 using the Astralux camera (Hippler et al. 2009) on the New Technology Telescope (NTT) at LSO on 2015/12/23. These observations are part of a campaign to detect potential companions for exoplanet host star candidates and place upper limits on magnitude contrasts. The data were taken using the SDSS z' filter, resulting in a set of 10^4 images with an exposure time of 100 ms each. We used the Drizzle algorithm from Fruchter & Hook (2002) to combine a set of the best 10% of images acquired and the result of these can be found in Figure 5, where we show the 1 and 4 arcsec radii lines for reference. A slightly asymmetric extended profile is visible on this image likely due to instrumental effects, confirmed by taking images of other targets on different nights that show a similar feature. As such, while we can confirm that there is no clear bright star in the vicinity of our target, we can not completely exclude the possibility that a faint close companion within 1" is not present. This is a generic problem with most confirmed transiting planets, and as such we further address this issue in Section 3.2 where we perform a blend analysis that increases our confidence that this is indeed a planetary body companion.

3. ANALYSIS

3.1. *Properties of the parent star*

We used the Zonal Atmospheric Stellar Parameter Estimator (ZASPE; Brahm et al. 2016a) to model the stellar parameters of the host stars for all targets. ZASPE is capable of precise stellar atmospheric parameter estimation from high-resolution echelle spectra from FGK-type stars. It compares the observed spectrum with a grid of synthetic spectra by a least squares minimisation of the normalised continuum in only the most sensitive regions of the stellar spectrum. The complete FGK-type star parameter space is searched using this method. We note that we do not treat micro and macroturbulence as free parameters, but instead assume that these values are a function of atmospheric parameters and apply modifications to the synthetic spectra accordingly. To take into account the microturbulence dependence of the line widths, we computed an empirical relation between the microturbulence and the stellar parameters. In particular, we used the stellar parameters provided by the SweetCat (Santos et al. 2013) catalogue to define a polynomial that delivers the microturbulence as function of $T_{\rm eff}$ and $\log g_\star$. Then, the macroturbulence value used in the synthetization of each spectrum was obtained using that empirical function. More details on this method

Table 2
Summary of spectroscopy observations

Instrument	UT Date(s)	# Spec.	Res. $\Delta\lambda/\lambda/1000$	S/N Range[a]	$\gamma_{\rm RV}$[b] ($\rm km\,s^{-1}$)	RV Precision[c] ($\rm m\,s^{-1}$)
HATS-22						
ESO 3.6 m/HARPS	2015 Feb–Apr	4	115	8–18	-7.370	15
Euler 1.2 m/CORALIE	2015 Feb–Jun	7	60	10–14	-7.414	35
ANU 2.3 m/WiFeS	2015 Feb 28	1	3	44	...	...
ANU 2.3 m/WiFeS	2015 Feb–Mar	2	7	63–83	-7.7	4000
MPG 2.2 m/FEROS	2015 Apr–Jun	4	48	43–58	-7.438	25
HATS-23						
ANU 2.3 m/WiFeS	2015 Jun 1	1	3	43	...	...
ANU 2.3 m/WiFeS	2015 Jun 1	1	7	39	-13.8	4000
MPG 2.2 m/FEROS	2015 Jun 8–18	8	48	18–39	-13.372	16
HATS-24						
ANU 2.3 m/WiFeS	2015 Feb 1	1	3	29	...	...
ANU 2.3 m/WiFeS	2015 Feb 1–5	3	7	31–55	-7.1	4000
ESO 3.6 m/HARPS	2015 Apr 6–7	2	115	9–15	-3.370	120
AAT 3.9 m/CYCLOPS2+UCLES [d]	2015 May 6–13	11	70	10–27	-3.284	160
Euler 1.2 m/CORALIE	2015 Jun 6–8	3	60	14–17	-3.236	140
MPG 2.2 m/FEROS	2015 Jun 17–21	4	48	42–60	-3.259	43

[a] S/N per resolution element near 5180 Å.
[b] For high-precision radial velocity observations included in the orbit determination this is the zero-point radial velocity from the best-fit orbit. For other instruments it is the mean value. We do not provide this quantity for the lower resolution WiFeS observations which were only used to measure stellar atmospheric parameters.
[c] For high-precision radial velocity observations included in the orbit determination this is the scatter in the radial velocity residuals from the best-fit orbit (which may include astrophysical jitter), for other instruments this is either an estimate of the precision (not including jitter), or the measured standard deviation. We do not provide this quantity for low-resolution observations from the ANU 2.3 m/WiFeS.
[d] We excluded from the analysis two of the AAT 3.9 m/CYCLOPS2+UCLES observations of HATS-24 which were taken during transit.

Table 3
Light curve data for HATS-22, HATS-23 and HATS-24.

Object[a]	BJD[b] (2,400,000+)	Mag[c]	$\sigma_{\rm Mag}$	Mag(orig)[d]	Filter	Instrument
HATS-22	56443.36356	−0.00627	0.00463	...	r	HS
HATS-22	56363.07603	0.00598	0.00473	...	r	HS
HATS-22	56466.97802	−0.00407	0.00561	...	r	HS
HATS-22	56396.13657	0.00730	0.00502	...	r	HS
HATS-22	56438.64228	−0.00929	0.00545	...	r	HS
HATS-22	56424.47483	−0.00012	0.00467	...	r	HS
HATS-22	56315.85060	−0.01903	0.00429	...	r	HS
HATS-22	56443.36694	0.01129	0.00468	...	r	HS
HATS-22	56424.47573	0.01945	0.00459	...	r	HS
HATS-22	56386.69363	0.01108	0.00455	...	r	HS

Note. — This table is available in a machine-readable form in the online journal. A portion is shown here for guidance regarding its form and content.
[a] Either HATS-22, HATS-23 or HATS-24.
[b] Barycentric Julian Date is computed directly from the UTC time without correction for leap seconds.
[c] The out-of-transit level has been subtracted. For observations made with the HATSouth instruments (identified by "HS" in the "Instrument" column) these magnitudes have been corrected for trends using the EPD and TFA procedures applied *prior* to fitting the transit model. This procedure may lead to an artificial dilution in the transit depths. The blend factors for the HATSouth light curves are listed in Table 5. For observations made with follow-up instruments (anything other than "HS" in the "Instrument" column), the magnitudes have been corrected for a quadratic trend in time, and for variations correlated with up to three PSF shape parameters, fit simultaneously with the transit.
[d] Raw magnitude values without correction for the quadratic trend in time, or for trends correlated with the seeing. These are only reported for the follow-up observations.

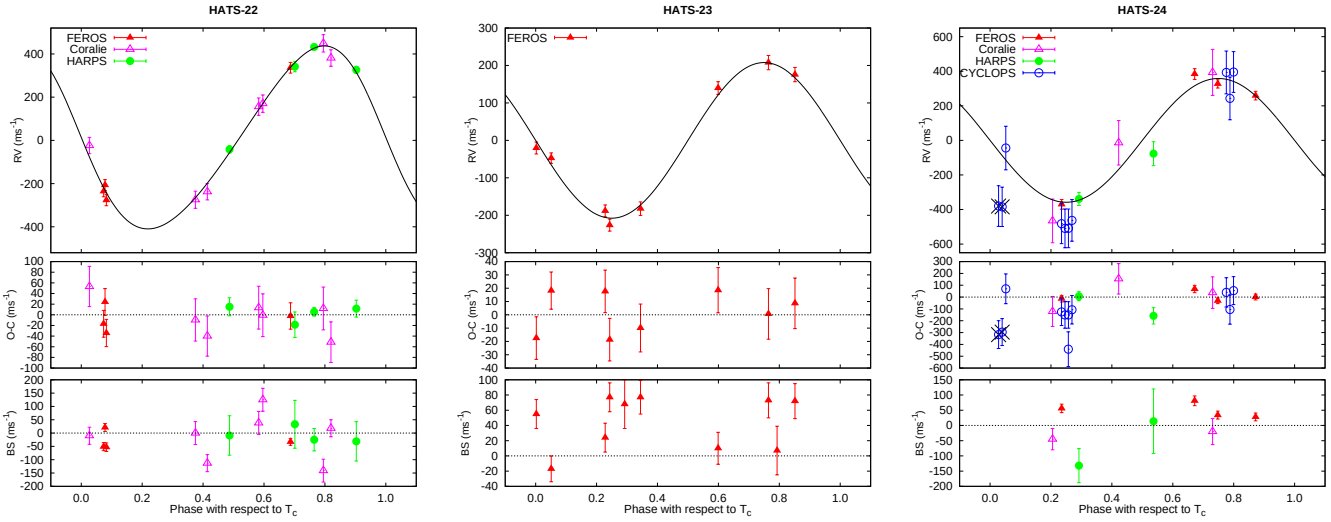

Figure 3. Phased high-precision radial velocity measurements for HATS-22 (left), HATS-23 (middle), and HATS-24 (right). The instruments used are labelled in the plots. For HATS-24 two observations marked with an X were obtained (partially) in transit and have been excluded from the analysis. In each case we display three panels. The top panel shows the phased measurements together with our best-fit model (see Table 5) for each system where we show the RV jitter values for each case. Zero-phase corresponds to the time of mid-transit. The center-of-mass velocity has been subtracted. The second panel displays the velocity $O-C$ residuals from the best fit. The error bars include the jitter terms listed in Table 5 added in quadrature to the formal errors for each instrument. The third panel shows the bisector spans (BS). Note the different vertical scales of the panels.

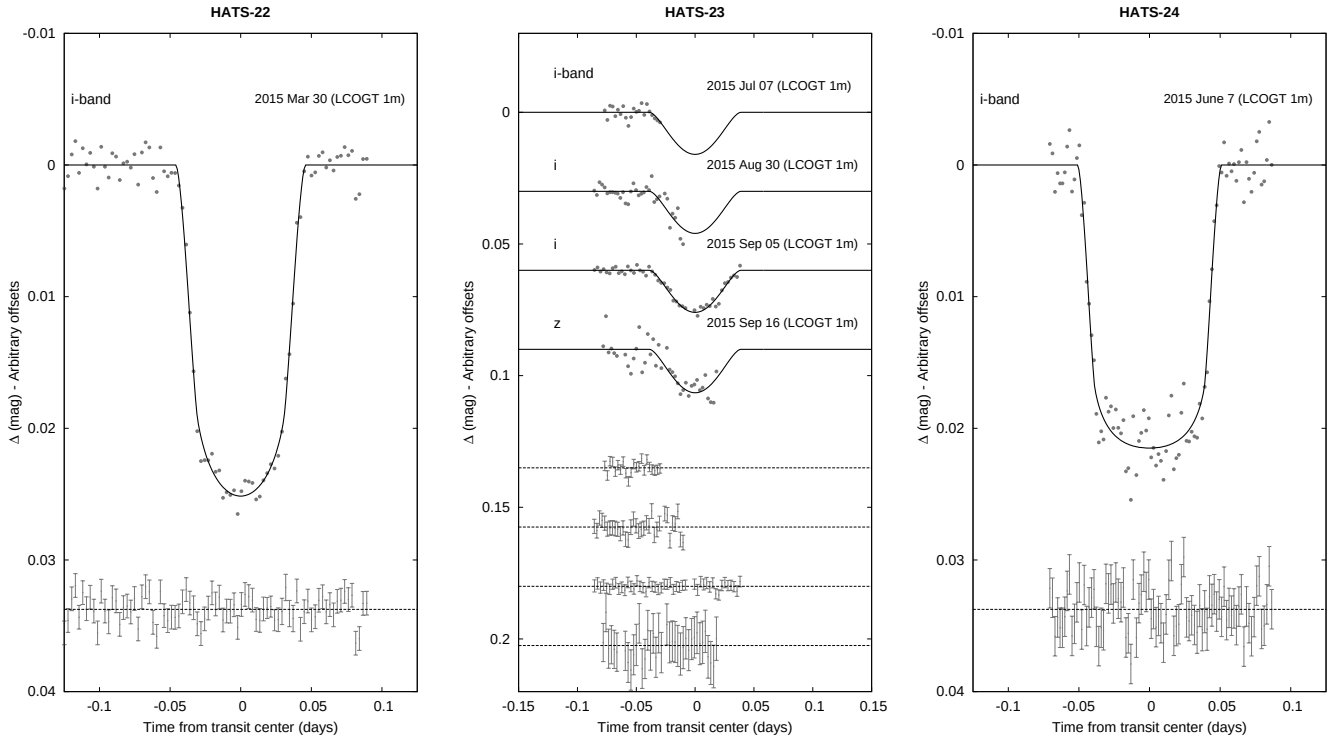

Figure 4. Unbinned transit light curves for HATS-22 (left), HATS-23 (middle) and HATS-24 (right). The light curves have been corrected for quadratic trends in time, and linear trends with up to three parameters characterizing the shape of the PSF, fitted simultaneously with the transit model. The dates of the events, filters and instruments used are indicated. Light curves following the first are displaced vertically for clarity. Our best fit from the global modeling described in Section 3.3 is shown by the solid lines. The residuals from the best-fit model are shown below in the same order as the original light curves. The error bars represent the photon and background shot noise, plus the readout noise.

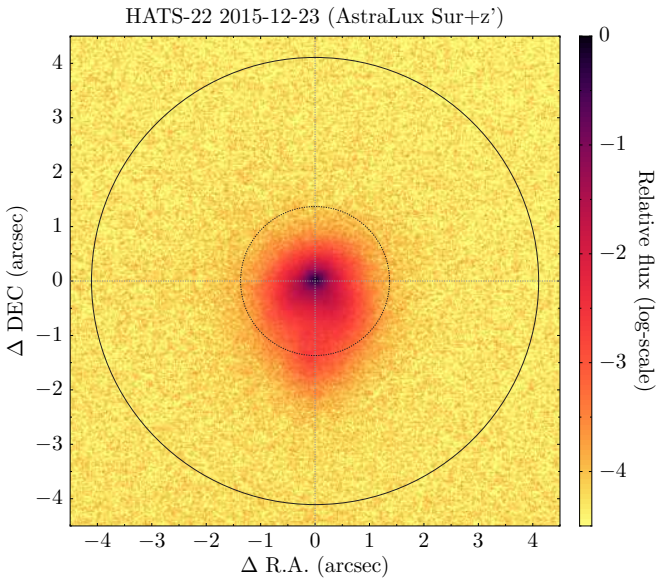

Figure 5. *Left* Lucky imaging observations of HATS-22 with the Astralux camera on the NTT telescope at La Silla in the z' band. We show the 1" and 4" radii lines for reference as well as the fitted centre of the star from the PSF modelling process. We note that the asymmetrical shape of the PSF is due to an instrumental effect related to non-stable focus on the telescope through the night. Similar patterns can be seen in other observations of this kind at similar times during the night.

can be found in Brahm et al. (2016a). This software used the combined spectra from the FEROS spectrograph taken for radial velocity purposes. We calculate an initial estimate of the effective temperature ($T_{\rm eff}$), the surface gravity ($\log g$), metallicity ([Fe/H]) and projected stellar rotational velocity of the stars ($v \sin i$) and then use the Yonsei-Yale (Y2; Yi et al. 2001) isochrones to obtain the remaining physical parameters. We do not, however, search for the best isochrone using the $\log g_\star$ but instead use the stellar density $\rho_\star$, which is well constrained by the photometric transit data and fitting routine. We then run the full set of parameters once again through a second iteration of ZASPE using the revised $\log g_\star$ to improve the results. We present the adopted results and an extensive set of host star parameters from several sources in Table 4. We find HATS-22 to be a $V = 13.455 \pm 0.040$ magnitude solar metallicity K-type star with $T_{\rm eff} = 4803 \pm 55$ K and sub-solar mass and radius ($M_\star = 0.759 \pm 0.019\ M_\odot$ and $R_\star = 0.689^{+0.028}_{-0.018}\ R_\odot$). HATS-23 ($V = 13.901 \pm 0.010$) and HATS-24 ($V = 12.830 \pm 0.010$) are determined to have super-solar masses and radii ($M_\star = 1.115 \pm 0.054\ M_\odot$; $R_\star = 1.145 \pm 0.070\ R_\odot$ and $M_\star = 1.218 \pm 0.036\ M_\odot$; $R_\star = 1.194^{+0.066}_{-0.041}\ R_\odot$ respectively). HATS-23 is a G-type with a $T_{\rm eff}$ of 5780 ± 120 K and [Fe/H] of 0.280 ± 0.070 whilst HATS-24 is a solar metallicity F-type star with determined $T_{\rm eff} = 6346 \pm 81$ K.

Distances to these stars were determined by comparing the measured broad-band photometry listed in Table 4 to the predicted magnitudes in each filter from the isochrones. We assumed a $R_V = 3.1$ extinction law from Cardelli et al. (1989) to determine the extinction and find these to be consistent within their uncertainties to reddening maps available on the NASA/IPAC infrared science archive [13]. The locations of each star on an $T_{\rm eff\star}$–$\rho_\star$ diagram (similar to a Hertzsprung-Russell diagram) are shown in Figure 6.

3.2. *Excluding blend scenarios*

In order to exclude blend scenarios we carried out an analysis following Hartman et al. (2012). We model the available photometric data (including light curves and catalog broad-band photometric measurements) for each object as a blend between an eclipsing binary star system and a third star along the line of sight. The physical properties of the stars are constrained using the Padova isochrones (Girardi et al. 2000), while we also require that the brightest of the three stars in the blend have atmospheric parameters consistent with those measured with ZASPE. We also simulate composite cross-correlation functions (CCFs) and use them to predict radial velocities and BSs for each blend scenario considered. For HATS-22 all blend scenarios tested can be rejected with greater than 3σ confidence, based on the photometry alone. Those models which cannot be rejected with at least 5σ confidence would have obviously double-lined spectra, and would also have BS variations in excess of $1\,{\rm km\,s^{-1}}$. For HATS-23 all blend scenarios tested can be rejected with greater than 3.3σ confidence based on the photometry. Although some of the models which cannot be rejected with at least 5σ confidence do predict low amplitude BS and radial velocity variations, the simulated radial velocities do not reproduce the sinusoidal variation with the orbital period that is clearly detected (Figure 3). For HATS-24 all blend scenarios tested can be rejected with greater than 4σ confidence based on the photometry. Those that cannot be rejected with at least 5σ confidence yield large amplitude radial velocity and BS variations in excess of $1\,{\rm km\,s^{-1}}$. We conclude that all three objects are transiting planet systems, however we cannot exclude the possibility that one or more of these objects is an unresolved binary stellar system with one component hosting a short period transiting planet (see Section 2.4). For the remainder of the paper we assume that these are all single stars with transiting planets, but we note that the radii, and potentially the masses, of the planets would be larger than what we infer here if subsequent observations reveal binary star companions.

3.3. *Global modeling of the data*

We modeled the HATSouth photometry, the follow-up photometry, and the high-precision radial velocity measurements following Pál et al. (2008); Bakos et al. (2010); Hartman et al. (2012). We fit Mandel & Agol (2002) transit models to the light curves, allowing for a dilution of the HATSouth transit depth as a result of blending from neighboring stars and over-correction by the trend-filtering method. To correct for systematic errors in the follow-up light curves we include in our model, for each event, a quadratic trend in time. Linear trends with up to three parameters describing the position and shape of the PSF are also included to compensate for any systematic effects due to poor guiding or PSF shape

[13] Publicly available at http://irsa.ipac.caltech.edu/applications/DUST/

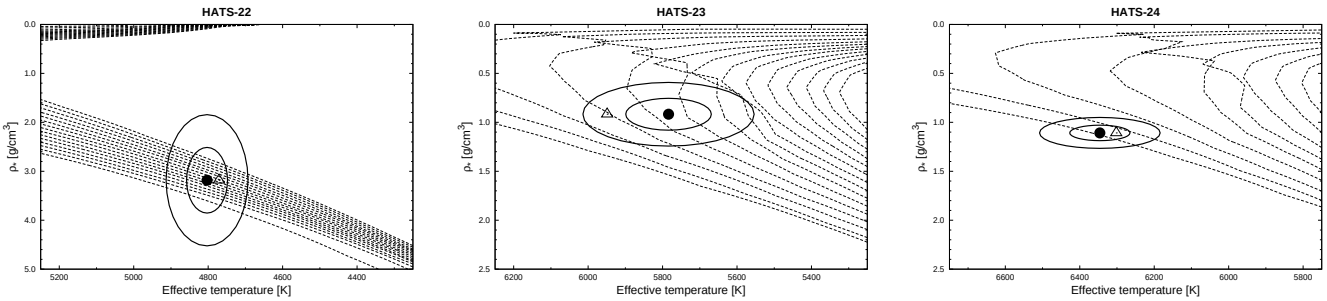

Figure 6. Model isochrones from Yi et al. (2001) for the measured metallicities of HATS-22 (left), HATS-23 (middle), and HATS-24 (right). We show models for ages of 0.2 Gyr and 1.0 to 14.0 Gyr in 1.0 Gyr increments (ages increasing from left to right). The adopted values of $T_{\rm eff\star}$ and $\rho_\star$ are shown together with their 1σ and 2σ confidence ellipsoids. The initial values of $T_{\rm eff\star}$ and $\rho_\star$ from the first ZASPE and light curve analyses are represented with a triangle.

changes throughout the transit observation. We fit Keplerian orbits to the radial velocity curves allowing the zero-point for each instrument to vary independently in the fit, and allowing for radial velocity jitter which we also vary as a free parameter for each instrument. We used a Differential Evolution Markov Chain Monte Carlo procedure to explore the fitness landscape and to determine the posterior distribution of the parameters.

We tried to both fit fixed circular orbit models and models with the eccentricity as a free parameter and then used the method of Weinberg et al. (2013) to estimate the Bayesian evidence for each scenario. We find a higher evidence for a non-circular orbital solution (by a factor of 80) for HATS-22b and find the most likely eccentricity to be $e = 0.079 \pm 0.026$. For HATS-23b and HATS-24b the fixed circular orbit models have the higher evidence; for HATS-23 the circular model has an evidence that is 20 times greater than the free-eccentricity model, while for HATS-24b the circular model has an evidence that is 70 times greater. We therefore adopt the parameters from the circular orbit models for these two systems, placing 95% confidence upper limits on their eccentricity as $e < 0.114$ and $e < 0.242$, respectively. The results of the fitting routines for each planet can be found in Table 5.

The grazing nature of HATS-23b naturally leads to a higher uncertainty on the determination of specific parameters typically constrained by the depth and shape of the transit. As a consequence of this, in Table 5 we have indicated the best fit results (with the corresponding 1σ confidence) as well as lower limits for selected parameters. In particular, the poor constraint on the impact parameter from the photometric follow-up light curves should be noted. This in turn affects the estimates of the orbital inclination, the planet radius and orbital separation. We also note that the larger uncertainties in the bottom light curve, for this planet are due to the fact that the data were taken in the z band. Whilst inclusion of these data in the transit fitting process has a minimal impact on the parameter estimation, the blend scenario analysis process (c.f. Section 3.2) benefited from this data set. The consistency between this partial transit with those observing in the i band limits the range of blend models which can fit the observations. Nevertheless, significantly higher precision multi-band follow-up would be required to improve the characterization of this system.

4. DISCUSSION

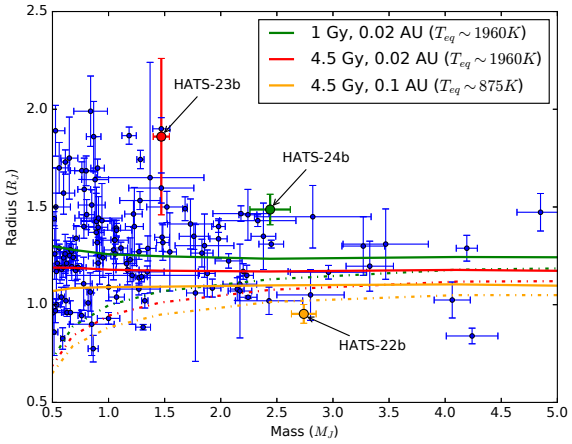

Figure 7. Mass-radius relation for hot Jupiters , defined as those planets with masses higher than $0.5M_{\rm J}$ and periods shorter than 10 days. We show theoretical models for planet structures from Fortney et al. (2007) for each of the three planets announced in this paper for both no core (solid lines) and $100M_\oplus$ core (dashed lines) scenarios. The new HATSouth planets are indicated. 4.5 Gy 0.1 AU models are shown for comparison with HATS-22b (yellow lines). The 4.5Gy 0.02 AU models (red lines) are used as equivalent examples for HATS-23b and the models for HATS-24b (1 Gy 0.02 AU) is shown in green lines.

In this work we report the discovery of three new moderately high-mass hot Jupiters by the HATSouth survey: HATS-22b, HATS-23b and HATS-24b. These planets add to the growing numbers of known hot Jupiters and provide vital additional insights into the formation and distribution of short-period massive planets. In Figures 7 and 8 we show these discoveries in the context of known planets with masses higher than $0.5M_{\rm J}$ and less than 10 day orbital periods [14].

4.1. *Mass-radius relation*

In Figure 7 we plot a mass-radius relation for known hot Jupiters , highlighting our three new discovered planets. Additionally, this plot contains a selection of predicted mass-radius relations from Fortney et al. (2007) that are closest to the conditions of each of these planets. For HATS-23b and HATS-24b (red and green curves respectively) we have selected those models that most

[14] Previously known planets taken from the NASA Exoplanet Archive at http://exoplanetarchive.ipac.caltech.edu/ on 02/02/2017

Table 4
Stellar parameters for HATS-22, HATS-23 and HATS-24

Parameter	**HATS-22** Value	**HATS-23** Value	**HATS-24** Value	Source
Astrometric properties and cross-identifications				
2MASS-ID	2MASS 11360233-2932359	2MASS 19052800-5004024	2MASS 17553376-6144503	
GSC-ID	GSC 6664-00373	GSC 8382-01464	GSC 9054-00129	
R.A. (J2000)	$11^{\rm h}36^{\rm m}02.16$s	$19^{\rm h}05^{\rm m}27.96$s	$17^{\rm h}55^{\rm m}33.60$s	2MASS
Dec. (J2000)	$-29°32'35.9''$	$-50°04'02.5''$	$-61°44'50.3''$	2MASS
$\mu_{\rm R.A.}$ (mas yr^{-1})	27.1 ± 1.1	3.3 ± 1.4	2.9 ± 2.6	UCAC4
$\mu_{\rm Dec.}$ (mas yr^{-1})	-8.7 ± 1.4	-1.1 ± 1.5	-11.0 ± 2.6	UCAC4
Spectroscopic properties				
$T_{\rm eff\star}$ (K)	4803 ± 55	5780 ± 120	6346 ± 81	ZASPE[a]
[Fe/H] (dex)	0.000 ± 0.040	0.280 ± 0.070	0.000 ± 0.050	ZASPE
$v \sin i$ (km s^{-1}) ...	0.50 ± 0.50	4.62 ± 0.49	9.44 ± 0.21	ZASPE
$v_{\rm mac}$ (km s^{-1})	2.49	4.00	4.87	Assumed
$v_{\rm mic}$ (km s^{-1})	0.58	1.08	1.56	Assumed
$\gamma_{\rm RV}$ (m s^{-1})	-7370 ± 23	-13372.0 ± 6.1	-3259 ± 41	CORALIE or FEROS[b]
Photometric properties				
B (mag).....	14.496 ± 0.040	14.625 ± 0.010	13.404 ± 0.010	APASS[c]
V (mag).....	13.455 ± 0.040	13.901 ± 0.010	12.830 ± 0.010	APASS[c]
g (mag)	13.943 ± 0.030	14.246 ± 0.010	13.071 ± 0.010	APASS[c]
r (mag)	13.056 ± 0.030	13.735 ± 0.010	12.643 ± 0.010	APASS[c]
i (mag).....	12.82 ± 0.14	13.427 ± 0.010	12.518 ± 0.090	APASS[c]
J (mag).....	11.556 ± 0.023	12.636 ± 0.025	11.678 ± 0.022	2MASS
H (mag)	11.006 ± 0.022	12.293 ± 0.025	11.447 ± 0.025	2MASS
K_s (mag)	10.942 ± 0.019	12.262 ± 0.030	11.382 ± 0.023	2MASS
Derived properties				
$M_\star$ ($M_\odot$)	0.759 ± 0.019	1.121 ± 0.046	1.212 ± 0.033	YY+$\rho_\star$+ZASPE [d]
$R_\star$ ($R_\odot$)	$0.689^{+0.028}_{-0.018}$	$1.199^{+0.061}_{-0.081}$	1.172 ± 0.033	YY+$\rho_\star$+ZASPE
$\log g_\star$ (cgs)	4.644 ± 0.028	4.328 ± 0.044	4.384 ± 0.021	YY+$\rho_\star$+ZASPE
$\rho_\star$ (g cm^{-3}) [e]	3.26 ± 0.68	$0.92^{+0.20}_{-0.11}$	$1.096^{+0.059}_{-0.085}$	Light curves
$\rho_\star$ (g cm^{-3}) [e]	$3.28^{+0.25}_{-0.39}$	$0.91^{+0.20}_{-0.11}$	1.059 ± 0.075	YY+Light curves+ZASPE
$L_\star$ ($L_\odot$).....	$0.226^{+0.026}_{-0.020}$	1.43 ± 0.22	1.96 ± 0.18	YY+$\rho_\star$+ZASPE
M_V (mag).....	6.71 ± 0.13	4.43 ± 0.18	4.03 ± 0.10	YY+$\rho_\star$+ZASPE
M_K (mag,ESO) ..	4.359 ± 0.081	2.90 ± 0.13	2.844 ± 0.065	YY+$\rho_\star$+ZASPE
Age (Gyr).....	... [f]	4.2 ± 1.5	$0.88^{+0.67}_{-0.45}$	YY+$\rho_\star$+ZASPE
A_V (mag).....	0.151 ± 0.084	0.106 ± 0.075	0.261 ± 0.061	YY+$\rho_\star$+ZASPE
Distance (pc).....	$207.9^{+8.9}_{-6.6}$	747 ± 46	510 ± 15	YY+$\rho_\star$+ZASPE

Note. — For each system we adopt the class of model which has the highest Bayesian evidence from among those tested. For HATS-23 and HATS-24 the adopted parameters come from a fit in which the orbit is assumed to be circular. For HATS-22 the eccentricity is allowed to vary.

[a] ZASPE = Zonal Atmospherical Stellar Parameter Estimator routine for the analysis of high-resolution spectra (Brahm et al. 2015, in preparation), applied to the FEROS spectra of HATS-22, HATS-23 and HATS-24. These parameters rely primarily on ZASPE, but have a small dependence also on the iterative analysis incorporating the isochrone search and global modeling of the data.

[b] This is based on CORALIE for HATS-22 and FEROS for HATS-23 and HATS-24. The error on $\gamma_{\rm RV}$ is determined from the orbital fit to the radial velocity measurements, and does not include the systematic uncertainty in transforming the velocities to the IAU standard system. The velocities have not been corrected for gravitational redshifts.

[c] From APASS DR6 (Henden et al. 2009) for as listed in the UCAC 4 catalog (Zacharias et al. 2012).

[d] YY+$\rho_\star$+ZASPE = Based on the YY isochrones (Yi et al. 2001), $\rho_\star$ as a luminosity indicator, and the ZASPE results.

[e] In the case of $\rho_\star$ we list two values. The first value is determined from the global fit to the light curves and radial velocity data, without imposing a constraint that the parameters match the stellar evolution models. The second value results from restricting the posterior distribution to combinations of $\rho_\star$+$T_{\rm eff\star}$+[Fe/H] that match to a YY stellar model.

[f] Omitted due to large uncertainty. Isochrone models (c.f. Figure 6) are unable to constrain age for this system.

closely matched the determined age and orbital separation of the planets (4.5 and 1 Gy respectively at 0.02 au separation) and with orbital periods of less than 10 days. These models assume a solar analogue host star and solar luminosity. For HATS-22b, however, due to the lower luminosity of the host star, we have selected the curve that most closely matches the expected equilibrium temperature T_{eq} for this planet, a 4.5 Gy model at 0.1 au, which is equivalent to a T_{eq} of approximately 875K, thereby matching the model to the planet's conditions. In all cases, we plot the two extreme limits of planetary core mass: no core (solid line) and a $100 M_\oplus$ core model (dashed line). Despite the fact that none of the target's radii fall within their equivalent predicted mass-radius range from the model curves, HATS-22b is consistent with a high-mass ($100 M_\oplus$) core at a 95% confidence level. This places this planet among the twenty highest bulk density hot Jupiters known to date, defined as those with masses higher than $0.5 M_{\rm J}$ and less than 10 day orbital periods. While we are not able to confidently make any conclusions regarding the structure of grazing transiting planet HATS-23b, we note that even assuming

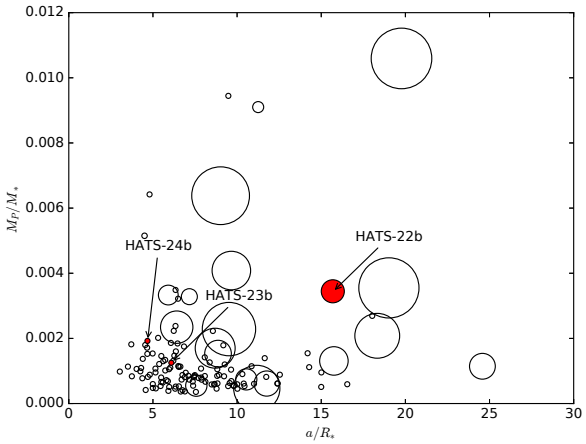

Figure 8. Planet to star mass ratio as a function of the ratio between the orbital separation and the stellar radius for known hot Jupiters . We have labelled our new discoveries in the plot, which are marked in filled red symbols. The dot sizes correspond to the planets' measured eccentricity ranging from zero (smallest size) up to a value of 0.562.

the lower limit on the radius of this planet at $1.31M_{\rm J}$ it is still more likely that this is an example of a low core mass hot Jupiter .

Perhaps the most interesting case in this context is that of HATS-24b. The radius of this planet is estimated more than 3σ above the model line for a pure helium-hydrogen planet at approximately this age and orbital separation. The short period and young age of the host star leads to a high equilibrium temperature ($T_{eq} = 2067 \pm 39K$), which puts it in a similar regime to other inflated hot Jupiters (e.g. WASP-71b (Smith et al. 2013) and HATS-35b (de Val-Borro et al. 2016)). As noted by Marley et al. (2007) and Fortney et al. (2007), the physical properties of giant planets at young ages are uncertain, and the model shown does not include considerations on the formation mechanism. The somewhat inflated radius of this planet may be due to a combination of mechanisms discussed in Section 1. Additionally, the apparent higher radius may be due to an ongoing evaporation of the upper layers of the planet's atmosphere as current models are unable to explain the radius of HATS-24b. This factor, coupled with the fact that the host star is moderately bright ($V = 12.830 \pm 0.010$) and the large transit depth signal, makes this a good target for further wavelength dependent transmission studies with large-class telescopes. Assuming a hydrogen dominated atmosphere, the scale height H for this planet is estimated at 314.8 ± 32.8 km, a value comparable to other inflated hot-Jupiters. Therefore, a transmission spectroscopic signal equivalent to 5 scale heights would be detectable at a level of ∼250ppm, well within the capability of current and future facilities.

4.2. *Eccentricity and tidal circularisation*

A comparative study between the three announced planets and previously known hot Jupiters is useful as the orbital eccentricity is an important parameter thought to be highly related to planetary migration both in disk interaction and planet scattering scenarios. As discussed in Section 1, eccentric orbits are found preferentially for higher mass planets (e.g. Southworth et al. 2009) and a higher the orbital separation seems to correspond with non-zero eccentricity (Pont et al. 2011). This supports the fact that a high mass planet at a large separation should require more time for tidal circularisation.

Our analysis (discussed in Section 3.3) finds HATS-22b to be the only planet of the three with a likely non-zero eccentricity of $e = 0.079 \pm 0.026$. The distinction between HATS-22b and the two other planets discovered in this work is made more evident in Figure 8, in which we have plotted the planet to stellar mass ratio as a function of the ratio between the orbital separation and the stellar radius (a/R_*). These parameters are the dominant factors in determining the tidal circularisation timescale of planetary orbits (Duffell & Chiang 2015; Ogilvie 2014) in which the mass ratio is proportional to the circularisation timescale. This is due to the fact that more massive planets are more likely to carve a large gap in the protoplanetary disk, leading to less efficient circularisation due to disk interaction. Thus, these planets should remain in moderate non-zero eccentric orbits for a longer time. In Figure 8 the dot sizes correspond to the eccentricity values, ranging from zero to 0.562, where the concentration of low or zero eccentricity planets, can be found for low values of both plotted parameters. HATS-22b can be seen occupying a region of parameter space clearly distinguished from that of HATS-23b and HATS-24b, suggesting that the eccentric orbit of HATS-22b may indeed be a result of insufficient time for full tidal circularisation. However, several examples can still be found in this figure which are inconsistent with this picture. The case of CoRoT-27b (Parviainen et al. 2014) is of a non-eccentric orbit planet that can be seen as the point with a mass ratio just under 0.01. Despite the moderate age of this system (4.21 ± 2.72 Gyr), a planet with such a high mass ratio is still predicted to be found in an eccetric orbit. On the other hand, several cases can also be found with low values of both parameters plotted in Figure 8 that still presently show detectable orbital eccentricity, suggesting that there are other mechanisms, besides tidal circularisation, determining the eccentricity distribution of exoplanets.

Development of the HATSouth project was funded by NSF MRI grant NSF/AST-0723074, operations have been supported by NASA grants NNX09AB29G and NNX12AH91H, and follow-up observations receive partial support from grant NSF/AST-1108686. A.J. acknowledges support from FONDECYT project 1130857, BASAL CATA PFB-06, and project IC120009 "Millennium Institute of Astrophysics (MAS)" of the Millenium Science Initiative, Chilean Ministry of Economy. R.B. and N.E. are supported by CONICYT-PCHA/Doctorado Nacional. R.B. and N.E. acknowledge additional support from project IC120009 "Millenium Institute of Astrophysics (MAS)" of the Millennium Science Initiative, Chilean Ministry of Economy. V.S. acknowledges support form BASAL CATA PFB-06. M.R. acknowledges support from FONDECYT postdoctoral fellowship 3120097. This work is based on observations made with ESO Telescopes at the La Silla Observatory. This paper also uses observations obtained with facilities of the Las Cumbres Observatory Global

Table 5
Orbital and planetary parameters for HATS-22b, HATS-23b and HATS-24b

Parameter	**HATS-22b** Value	**HATS-23b** Value	**HATS-24b** Value
Light curve parameters			
P (days)	4.7228124 ± 0.0000052	2.1605156 ± 0.0000045	1.3484954 ± 0.0000013
T_c (BJD) [a]	$2457078.58030 \pm 0.00022$	$2457072.85266 \pm 0.00070$	$2457038.47327 \pm 0.00038$
T_{14} (days) [a]	0.0913 ± 0.0015	0.0752 ± 0.0031	0.1008 ± 0.0010
$T_{12} = T_{34}$ (days) [a]	0.0154 ± 0.0014	0.094 ± 0.013	0.01241 ± 0.00081
$a/R_\star$	$15.70^{+0.39}_{-0.65}$	$6.08^{+0.41}_{-0.26}$	$4.67^{+0.10}_{-0.14}$
$\zeta/R_\star$ [b]	$26.09^{+0.28}_{-0.19}$	56^{+28}_{-13}	22.64 ± 0.17
$R_p/R_\star$	0.1426 ± 0.0025	0.159 ± 0.020	0.1307 ± 0.0030
b^2	$0.287^{+0.040}_{-0.064}$	$0.901^{+0.057}_{-0.090}$	$0.076^{+0.050}_{-0.045}$
b^2 lower limit [c]	...	> 0.771	...
$b \equiv a\cos i/R_\star$	$0.536^{+0.036}_{-0.064}$	$0.949^{+0.029}_{-0.049}$	$0.276^{+0.079}_{-0.101}$
b lower limit [c]	...	> 0.878	...
i (deg)	87.96 ± 0.21	$81.02^{+0.93}_{-0.62}$	86.6 ± 1.2
i upper limit (deg) [c]	...	< 83.5	...
HATSouth blend factors [d]			
Blend factor	0.861 ± 0.030	0.750 ± 0.062	0.787 ± 0.042
Limb-darkening coefficients [e]			
c_1, r	0.5808	0.3728	0.2638
c_2, r	0.1721	0.3215	0.3753
c_1, i	0.4355	0.2774	0.1919
c_2, i	0.2255	0.3334	0.3654
c_1, z	...	0.2116	...
c_2, z	...	0.3342	...
radial velocity parameters			
K ($\mathrm{m\,s^{-1}}$)	399 ± 15	212.3 ± 8.6	396 ± 29
e [f]	0.079 ± 0.026	< 0.114	< 0.242
ω (deg)	56 ± 73	...	...
$\sqrt{e}\cos\omega$	$0.168^{+0.046}_{-0.062}$	...	...
$\sqrt{e}\sin\omega$	$0.225^{+0.084}_{-0.126}$	...	...
$e\cos\omega$	$0.043^{+0.016}_{-0.011}$	...	...
$e\sin\omega$	0.061 ± 0.040	...	...
radial velocity jitter FEROS ($\mathrm{m\,s^{-1}}$) [g]	35 ± 28	0.0 ± 6.6	8 ± 52
radial velocity jitter HARPS ($\mathrm{m\,s^{-1}}$)	1 ± 41	...	60 ± 140
radial velocity jitter CORALIE ($\mathrm{m\,s^{-1}}$)	1 ± 41	...	70 ± 140
radial velocity jitter CYCLOPS2+UCLES ($\mathrm{m\,s^{-1}}$)	...	...	72 ± 55
Planetary parameters			
M_p (M_J)	2.74 ± 0.11	1.470 ± 0.072	2.44 ± 0.18
R_p (R_J)	$0.953^{+0.048}_{-0.029}$	$1.86^{+0.30}_{-0.40}$	$1.487^{+0.078}_{-0.054}$
R_p lower limit (R_J) [c]	...	> 1.31	...
$C(M_p, R_p)$ [h]	0.20	0.23	-0.18
ρ_p ($\mathrm{g\,cm^{-3}}$)	3.89 ± 0.45	$0.29^{+0.30}_{-0.10}$	0.92 ± 0.15
$\log g_p$ (cgs)	3.868 ± 0.036	$3.02^{+0.21}_{-0.12}$	3.435 ± 0.054
a (AU)	0.05025 ± 0.00042	0.03397 ± 0.00047	0.02547 ± 0.00023
T_eq (K)	858^{+24}_{-17}	1654 ± 54	2067 ± 39
Θ [i]	0.378 ± 0.020	$0.0475^{+0.0131}_{-0.0067}$	$0.0684^{+0.0092}_{-0.0070}$
$\log_{10}\langle F\rangle$ (cgs) [j]	$8.088^{+0.048}_{-0.036}$	9.228 ± 0.058	9.615 ± 0.033

Note. — For each system we adopt the class of model which has the highest Bayesian evidence from among those tested. For HATS-23b and HATS-24b the adopted parameters come from a fit in which the orbit is assumed to be circular. For HATS-22b the eccentricity is allowed to vary.

[a] Times are in Barycentric Julian Date calculated directly from UTC *without* correction for leap seconds. T_c: Reference epoch of mid transit that minimizes the correlation with the orbital period. T_{14}: total transit duration, time between first to last contact; $T_{12} = T_{34}$: ingress/egress time, time between first and second, or third and fourth contact.

[b] Reciprocal of the half duration of the transit used as a jump parameter in our Markov chain Monte Carlo (MCMC) analysis in place of $a/R_\star$. It is related to $a/R_\star$ by the expression $\zeta/R_\star = a/R_\star(2\pi(1 + e\sin\omega))/(P\sqrt{1-b^2}\sqrt{1-e^2})$ (Bakos et al. 2010).

[c] The grazing transits of HATS-23b mean that we cannot place a strong upper limit on the impact parameter. For this system we also provide 95% confidence lower limits on b^2, b and R_p, and the 95% confidence upper limit on i.

[d] Scaling factor applied to the model transit that is fit to the HATSouth light curves. This factor accounts for dilution of the transit due to blending from neighboring stars and over-filtering of the light curve. These factors are varied in the fit.

[e] Values for a quadratic law, adopted from the tabulations by Claret (2004) according to the spectroscopic (ZASPE) parameters listed in Table 4.

[f] For fixed circular orbit models we list the 95% confidence upper limit on the eccentricity determined when $\sqrt{e}\cos\omega$ and $\sqrt{e}\sin\omega$ are allowed to vary in the fit.

[g] Term added in quadrature to the formal radial velocity uncertainties for each instrument. This is treated as a free parameter in the fitting routine. In cases where the jitter is consistent with zero, we list its 95% confidence upper limit.

[h] Correlation coefficient between the planetary mass M_p and radius R_p estimated from the posterior parameter distribution.

[i] The Safronov number is given by $\Theta = \frac{1}{2}(V_\mathrm{esc}/V_\mathrm{orb})^2 = (a/R_p)(M_p/M_\star)$ (see Hansen & Barman 2007).

[j] Incoming flux per unit surface area, averaged over the orbit assuming a circular geometry.

Telescope. Work at the Australian National University is supported by ARC Laureate Fellowship Grant FL0992131. We acknowledge the use of the AAVSO Photometric All-Sky Survey (APASS), funded by the Robert Martin Ayers Sciences Fund, and the SIMBAD database, operated at CDS, Strasbourg, France. Operations at the MPG 2.2 m Telescope are jointly performed by the Max Planck Gesellschaft and the European Southern Observatory. The imaging system GROND has been built by the high-energy group of MPE in collaboration with the LSW Tautenburg and ESO. We thank Régis Lachaume for his technical assistance during the observations at the MPG 2.2 m Telescope. We thank Helmut Steinle and Jochen Greiner for supporting the GROND observations presented in this manuscript. We are grateful to P.Sackett for her help in the early phase of the HATSouth project. This research has made use of the NASA/ IPAC Infrared Science Archive, which is operated by the Jet Propulsion Laboratory, California Institute of Technology, under contract with the National Aeronautics and Space Administration. Observing time were obtained through proposals CN2013A-171, CN2013B-55, CN2014A-104, CN2014B-57, CN2015A-51 and ESO 096.C-0544.

REFERENCES

Addison, B. C., Tinney, C. G., Wright, D. J., et al. 2013, ApJ, 774, L9
Alibert, Y., Mordasini, C., Benz, W., & Winisdoerffer, C. 2005, A&A, 434, 343
Antonini, F., Hamers, A. S., & Lithwick, Y. 2016, ArXiv e-prints, 1604.01781
Bakos, G. Á., Torres, G., Pál, A., et al. 2010, ApJ, 710, 1724
Bakos, G. Á., Csubry, Z., Penev, K., et al. 2013, PASP, 125, 154
Batygin, K., Bodenheimer, P. H., & Laughlin, G. P. 2016, ApJ, 829, 114
Bayliss, D., Zhou, G., Penev, K., et al. 2013, AJ, 146, 113
Bayliss, D., Hartman, J. D., Bakos, G. Á., et al. 2015, AJ, 150, 49
Bento, J., Wheatley, P. J., Copperwheat, C. M., et al. 2014, MNRAS, 437, 1511
Bodenheimer, P., Hubickyj, O., & Lissauer, J. J. 2000, Icarus, 143, 2
Boss, A. P. 1995, Science, 267, 360
Brahm, R., Jordan, A., Hartman, J., & Bakos, G. 2016a, ArXiv e-prints, 1607.05792
Brahm, R., Jordán, A., Bakos, G. Á., et al. 2016b, AJ, 151, 89
Brown, T. M., Baliber, N., Bianco, F. B., et al. 2013, PASP, 125, 1031
Cardelli, J. A., Clayton, G. C., & Mathis, J. S. 1989, ApJ, 345, 245
Chambers, J. E. 2009, ApJ, 705, 1206
Claret, A. 2004, A&A, 428, 1001
Collier Cameron, A., Bruce, V. A., Miller, G. R. M., Triaud, A. H. M. J., & Queloz, D. 2010, MNRAS, 403, 151
Croll, B., Lafreniere, D., Albert, L., et al. 2011, AJ, 141, 30
de Val-Borro, M., Bakos, G. Á., Brahm, R., et al. 2016, AJ, 152, 161
Désert, J.-M., Charbonneau, D., Fortney, J. J., et al. 2011, ApJS, 197, 11
Donati, J. F., Moutou, C., Malo, L., et al. 2016, Nature, 534, 662
Dopita, M., Hart, J., McGregor, P., et al. 2007, Ap&SS, 310, 255
Duffell, P. C., & Chiang, E. 2015, ApJ, 812, 94
Ford, E. B., & Rasio, F. A. 2008, ApJ, 686, 621
Fortney, J. J., Marley, M. S., & Barnes, J. W. 2007, ApJ, 659, 1661
Fruchter, A. S., & Hook, R. N. 2002, PASP, 114, 144
Gandolfi, D., Collier Cameron, A., Endl, M., et al. 2012, A&A, 543, L5
Girardi, L., Bressan, A., Bertelli, G., & Chiosi, C. 2000, A&AS, 141, 371
Gustafsson, B., Edvardsson, B., Eriksson, K., et al. 2008, A&A, 486, 951
Hansen, B. M. S., & Barman, T. 2007, ApJ, 671, 861
Hartman, J. D., Bakos, G. Á., Béky, B., et al. 2012, AJ, 144, 139
Hartman, J. D., Bakos, G. Á., Buchhave, L. A., et al. 2015, AJ, 150, 197
Henden, A. A., Welch, D. L., Terrell, D., & Levine, S. E. 2009, in American Astronomical Society Meeting Abstracts, Vol. 214, American Astronomical Society Meeting Abstracts #214, #407.02
Hippler, S., Bergfors, C., Brandner Wolfgang, et al. 2009, The Messenger, 137, 14
Jordán, A., Espinoza, N., Rabus, M., et al. 2013, ApJ, 778, 184
Jordán, A., Brahm, R., Bakos, G. Á., et al. 2014, AJ, 148, 29
Kaufer, A., & Pasquini, L. 1998, in Society of Photo-Optical Instrumentation Engineers (SPIE) Conference Series, Vol. 3355, Optical Astronomical Instrumentation, ed. S. D'Odorico, 844–854
Knutson, H. A., Charbonneau, D., Allen, L. E., Burrows, A., & Megeath, S. T. 2008, ApJ, 673, 526
Kovács, G., Bakos, G., & Noyes, R. W. 2005, MNRAS, 356, 557
Kovács, G., Zucker, S., & Mazeh, T. 2002, A&A, 391, 369
Kozai, Y. 1962, AJ, 67, 591
Lissauer, J. J. 1995, Icarus, 114, 217
Lithwick, Y., & Wu, Y. 2011, ApJ, 739, 31
Louden, T., & Wheatley, P. J. 2015, ApJ, 814, L24
Mandel, K., & Agol, E. 2002, ApJ, 580, L171
Marcy, G. W., Butler, R. P., Vogt, S. S., et al. 2005, ApJ, 619, 570
Marley, M. S., Ackerman, A. S., Cuzzi, J. N., & Kitzmann, D. 2013, Clouds and Hazes in Exoplanet Atmospheres, ed. S. J. Mackwell, A. A. Simon-Miller, J. W. Harder, & M. A. Bullock, 367–391
Marley, M. S., Fortney, J. J., Hubickyj, O., Bodenheimer, P., & Lissauer, J. J. 2007, ApJ, 655, 541
Mayor, M., Pepe, F., Queloz, D., et al. 2003, The Messenger, 114, 20
Mazeh, T., Mayor, M., & Latham, D. W. 1997, ApJ, 478, 367
Ngo, H., Knutson, H. A., Hinkley, S., et al. 2016, ArXiv e-prints, 1606.07102
Ogilvie, G. I. 2014, ARA&A, 52, 171
Pál, A., Bakos, G. Á., Torres, G., et al. 2008, ApJ, 680, 1450
Parviainen, H., Gandolfi, D., Deleuil, M., et al. 2014, A&A, 562, A140
Penev, K., Bakos, G. Á., Bayliss, D., et al. 2013, AJ, 145, 5
Petrovich, C. 2015, ApJ, 805, 75
Pont, F., Husnoo, N., Mazeh, T., & Fabrycky, D. 2011, MNRAS, 414, 1278
Pont, F., Knutson, H., Gilliland, R. L., Moutou, C., & Charbonneau, D. 2008, MNRAS, 385, 109
Queloz, D., Mayor, M., Udry, S., et al. 2001, The Messenger, 105, 1
Rasio, F. A., & Ford, E. B. 1996, Science, 274, 954
Rice, W. K. M., Armitage, P. J., & Hogg, D. F. 2008, MNRAS, 384, 1242
Santos, N. C., Sousa, S. G., Mortier, A., et al. 2013, A&A, 556, A150
Schlaufman, K. C., & Winn, J. N. 2016, ArXiv e-prints, 1604.03107
Seager, S., & Sasselov, D. D. 2000, ApJ, 537, 916
Sing, D. K., Pont, F., Aigrain, S., et al. 2011, MNRAS, 416, 1443
Smith, A. M. S., Anderson, D. R., Bouchy, F., et al. 2013, A&A, 552, A120
Southworth, J., Hinse, T. C., Dominik, M., et al. 2009, ApJ, 707, 167
Struve, O. 1952, The Observatory, 72, 199
Weinberg, M. D., Yoon, I., & Katz, N. 2013, ArXiv e-prints, 1301.3156
Wu, Y., & Lithwick, Y. 2011, ApJ, 735, 109
Wu, Y., & Murray, N. 2003, ApJ, 589, 605
Yi, S., Demarque, P., Kim, Y.-C., et al. 2001, ApJS, 136, 417
Zacharias, N., Finch, C. T., Girard, T. M., et al. 2012, VizieR Online Data Catalog, 1322, 0
Zechmeister, M., & Kürster, M. 2009, A&A, 496, 577
Zhou, G., Bayliss, D. D. R., Kedziora-Chudczer, L., et al. 2014, MNRAS, 445, 2746

Zhou, G., Kedziora-Chudczer, L., Bayliss, D. D. R., & Bailey, J. 2013, ApJ, 774, 118
Zhou, G., Latham, D. W., Bieryla, A., et al. 2016, ArXiv e-prints, 1605.01991

Table 6
Relative radial velocities and bisector spans for HATS-22 and HATS-23.

BJD (2,450,000+)	RV[a] ($m\,s^{-1}$)	σ_{RV}[b] ($m\,s^{-1}$)	BS ($m\,s^{-1}$)	σ_{BS} ($m\,s^{-1}$)	Phase	Instrument
HATS-22						
7072.74688	432.36	8.00	−25.0	42.0	0.765	HARPS
7075.81290	−237.86	17.00	−113.0	32.0	0.414	CORALIE
7077.72945	381.14	18.00	18.0	32.0	0.820	CORALIE
7078.70639	−23.86	17.00	−10.0	32.0	0.027	CORALIE
7109.73325	170.14	22.00	125.0	43.0	0.596	CORALIE
7118.66166	−41.64	17.00	−9.0	74.0	0.487	HARPS
7119.60792	336.19	10.00	−33.0	13.0	0.687	FEROS
7119.67550	341.36	24.00	33.0	90.0	0.701	HARPS
7120.62753	326.36	16.00	−31.0	74.0	0.903	HARPS
7179.52938	−274.86	21.00	0.0	43.0	0.375	CORALIE
7180.51051	156.14	22.00	38.0	43.0	0.583	CORALIE
7181.51430	449.14	22.00	−141.0	43.0	0.795	CORALIE
7187.55141	−235.81	11.00	−51.0	15.0	0.073	FEROS
7187.57284	−206.81	11.00	21.0	15.0	0.078	FEROS
7187.59426	−276.81	12.00	−53.0	16.0	0.082	FEROS
HATS-23						
7181.62180	−182.31	18.00	77.0	22.0	0.344	FEROS
7182.71745	175.69	19.00	72.0	23.0	0.851	FEROS
7183.66969	···	···	68.0	32.0	0.292	FEROS
7184.75104	···	···	7.0	32.0	0.793	FEROS
7185.72406	−226.31	16.00	77.0	19.0	0.243	FEROS
7186.85044	207.69	19.00	73.0	23.0	0.764	FEROS
7187.85244	−188.31	16.00	24.0	19.0	0.228	FEROS
7189.63018	−47.31	14.00	−17.0	17.0	0.051	FEROS
7190.81426	139.69	17.00	10.0	21.0	0.599	FEROS
7191.68515	−20.31	16.00	55.0	19.0	0.002	FEROS
HATS-24						
7118.75825	−76.82	69.00	14.0	106.0	0.537	HARPS
7119.77652	−338.82	38.00	−132.0	56.0	0.292	HARPS
7149.08745[c]	−379.95	40.30	···	···	0.028	CYCLOPS
7149.10350[c]	−384.45	27.60	···	···	0.040	CYCLOPS
7149.11954	−44.25	61.00	···	···	0.052	CYCLOPS
7150.09608	393.15	56.20	···	···	0.776	CYCLOPS
7150.11204	242.95	55.80	···	···	0.788	CYCLOPS
7150.12799	395.45	41.60	···	···	0.799	CYCLOPS
7152.06340	−481.85	33.80	···	···	0.235	CYCLOPS
7152.07872	−509.25	21.00	···	···	0.246	CYCLOPS
7152.09403	−508.95	17.90	···	···	0.257	CYCLOPS
7156.13898	−798.25	96.80	···	···	0.257	CYCLOPS
7156.15505	−462.95	48.40	···	···	0.269	CYCLOPS
7179.70211	393.16	71.00	−20.0	43.0	0.731	CORALIE
7180.63482	−13.84	62.00	···	···	0.422	CORALIE
7181.69032	−465.84	57.00	−45.0	35.0	0.205	CORALIE
7190.68048	258.75	25.00	28.0	13.0	0.872	FEROS
7191.75911	383.75	31.00	81.0	16.0	0.672	FEROS
7193.86712	−370.25	28.00	56.0	14.0	0.235	FEROS
7194.55840	326.75	24.00	34.0	13.0	0.748	FEROS

Note. —

[a] The zero-point of these velocities is arbitrary. An overall offset γ_{rel} fitted independently to the velocities from each instrument has been subtracted.

[b] Internal errors excluding the component of astrophysical jitter considered in Section 3.3.

[c] These observations were excluded from the analysis because the observations were (partially) obtained with the planet in transit, and thus may be affected by the Rossiter-McLaughlin effect.

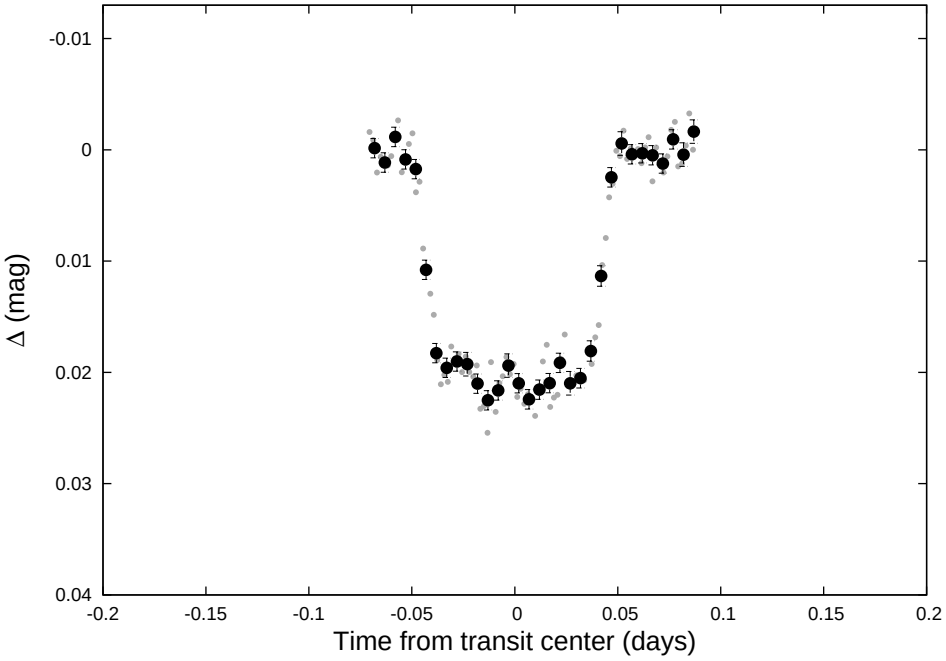
-0.01
0
0.01
0.02
0.03
0.04
Δ (mag)
-0.2
-0.15
-0.1
-0.05
0
0.05
0.1
0.15
0.2
Time from transit center (days)

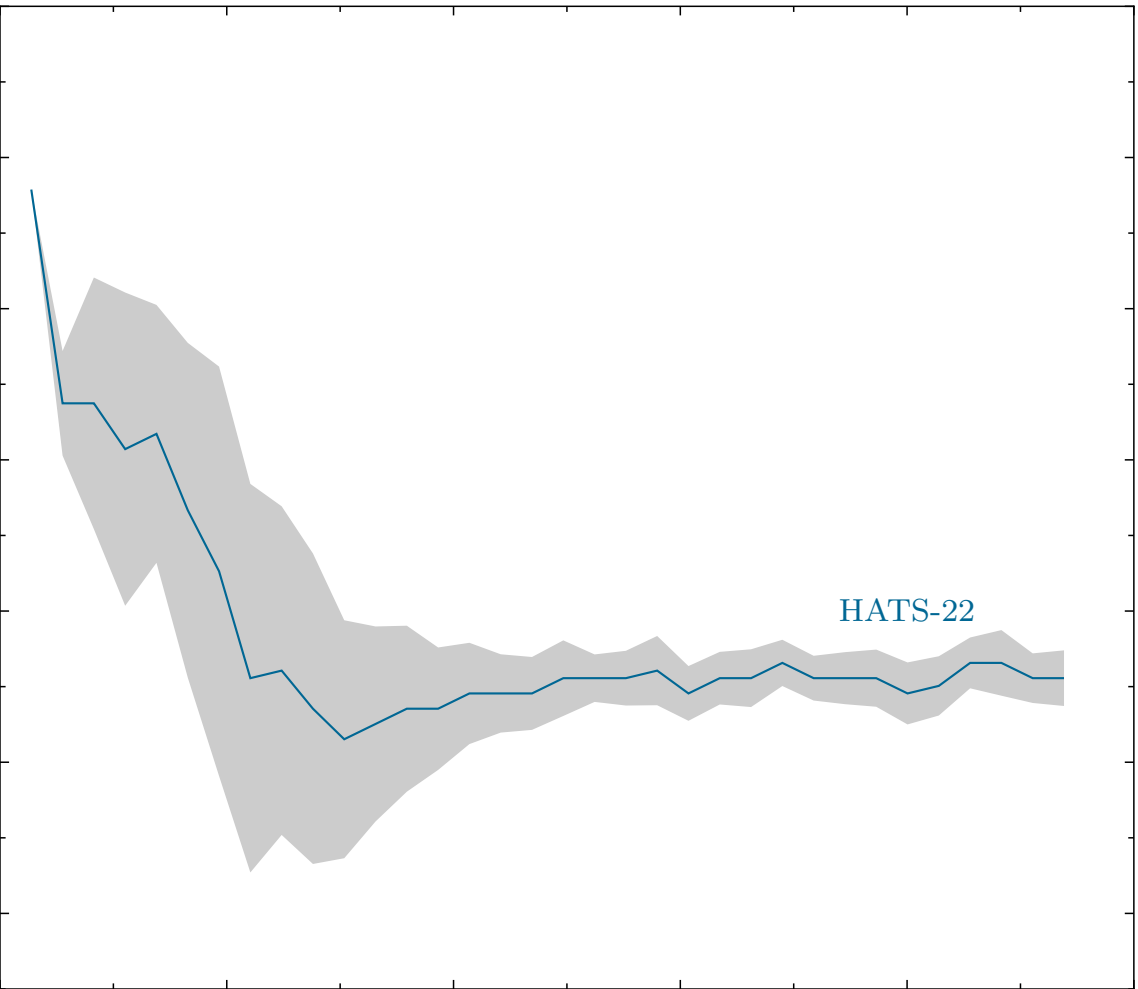
HATS-22

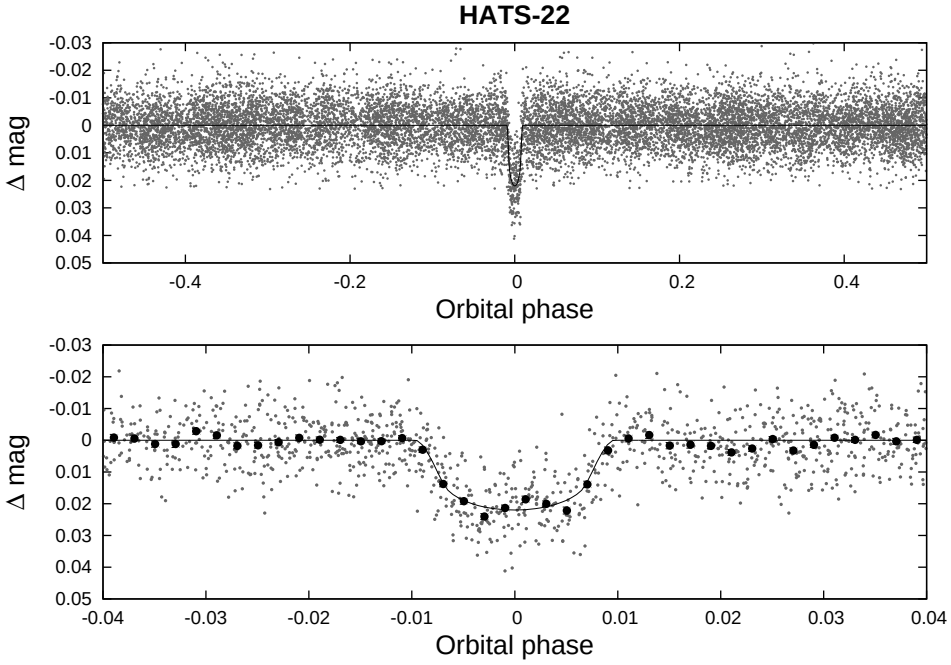
HATS-22
Δ mag
-0.03
-0.02
-0.01
0
0.01
0.02
0.03
0.04
0.05
-0.4
-0.2
0
0.2
0.4
Orbital phase
Δ mag
-0.03
-0.02
-0.01
0
0.01
0.02
0.03
0.04
0.05
-0.04
-0.03
-0.02
-0.01
0
0.01
0.02
0.03
0.04
Orbital phase

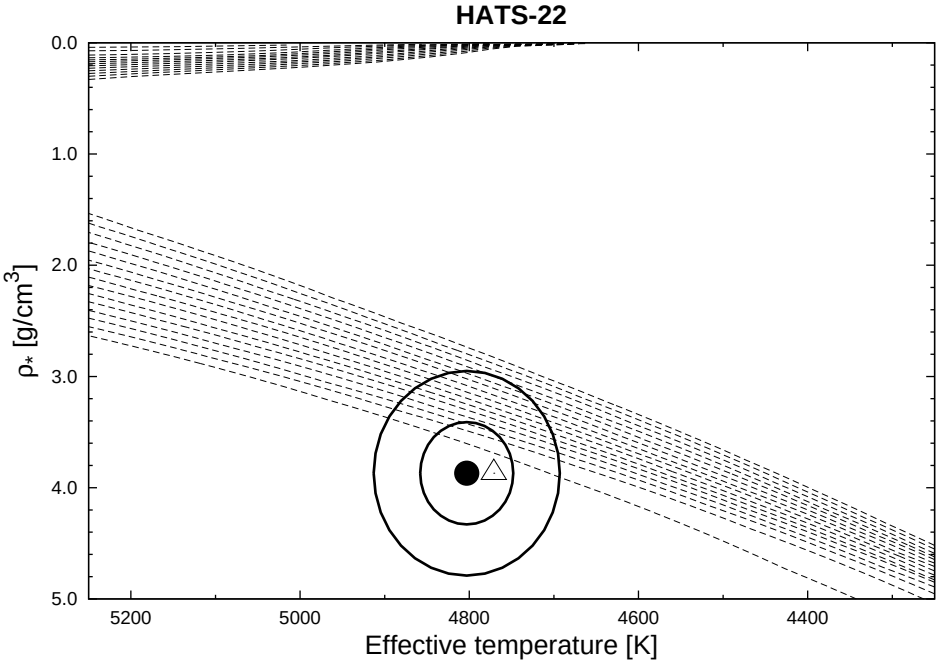
HATS-22
0.0
1.0
2.0
3.0
4.0
5.0
ρ* [g/cm3]
5200
5000
4800
4600
4400
Effective temperature [K]

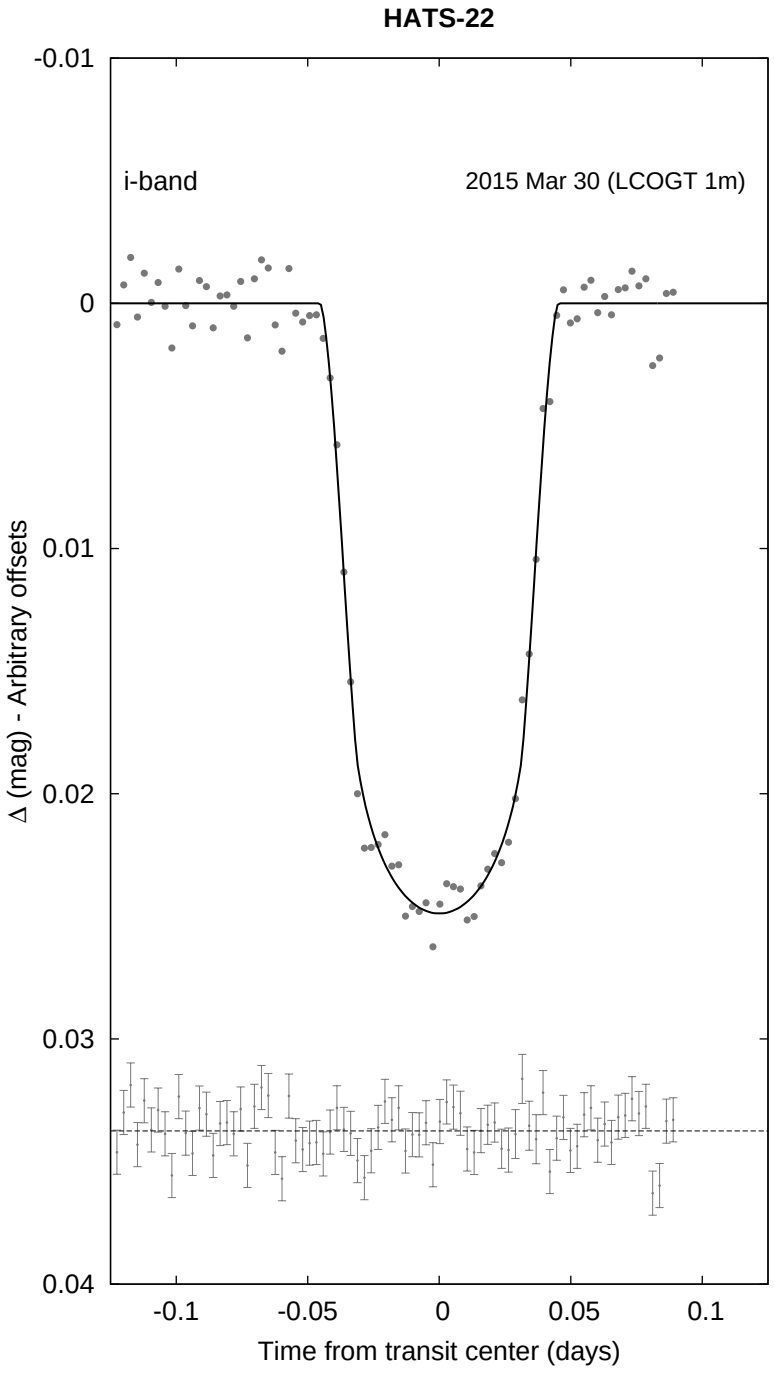
HATS-22
i-band
2015 Mar 30 (LCOGT 1m)
-0.01
0
0.01
0.02
0.03
0.04
Δ (mag) - Arbitrary offsets
-0.1
-0.05
0
0.05
0.1
Time from transit center (days)

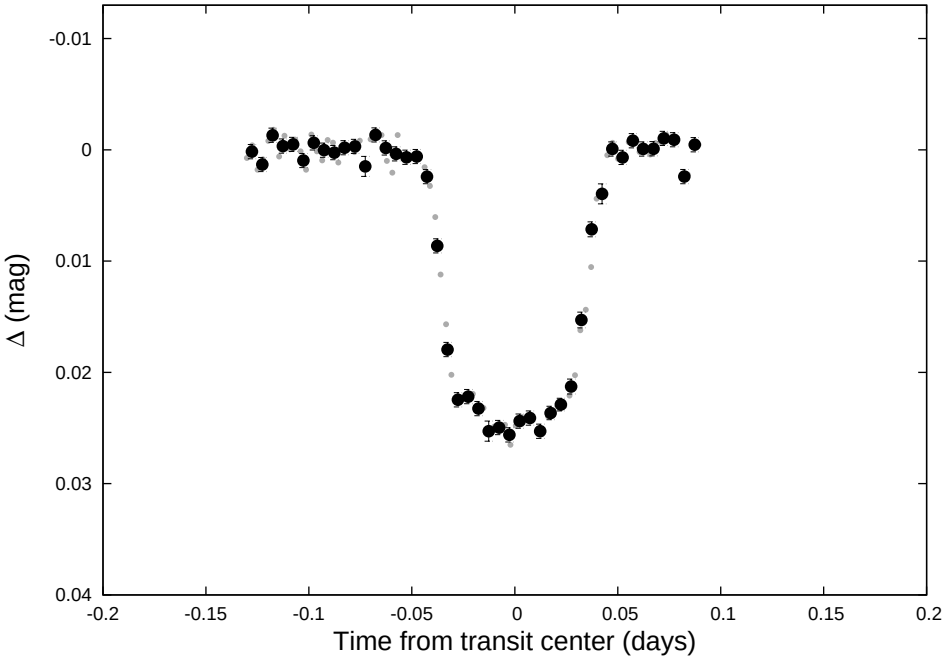
-0.01
0
0.01
0.02
0.03
0.04
Δ (mag)
-0.2
-0.15
-0.1
-0.05
0
0.05
0.1
0.15
0.2
Time from transit center (days)

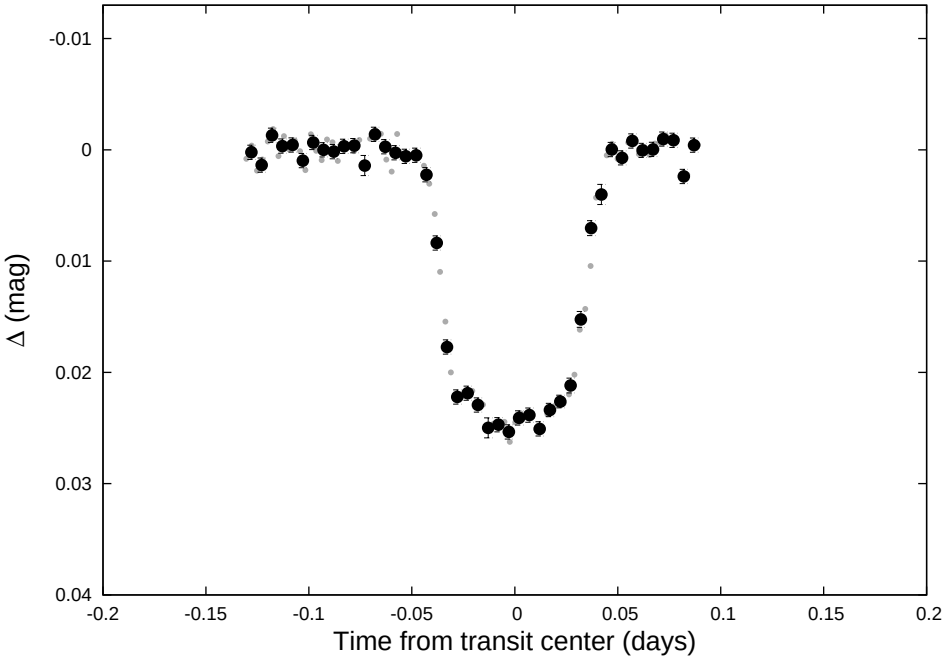
-0.01
0
0.01
0.02
0.03
0.04
Δ (mag)
-0.2
-0.15
-0.1
-0.05
0
0.05
0.1
0.15
0.2
Time from transit center (days)

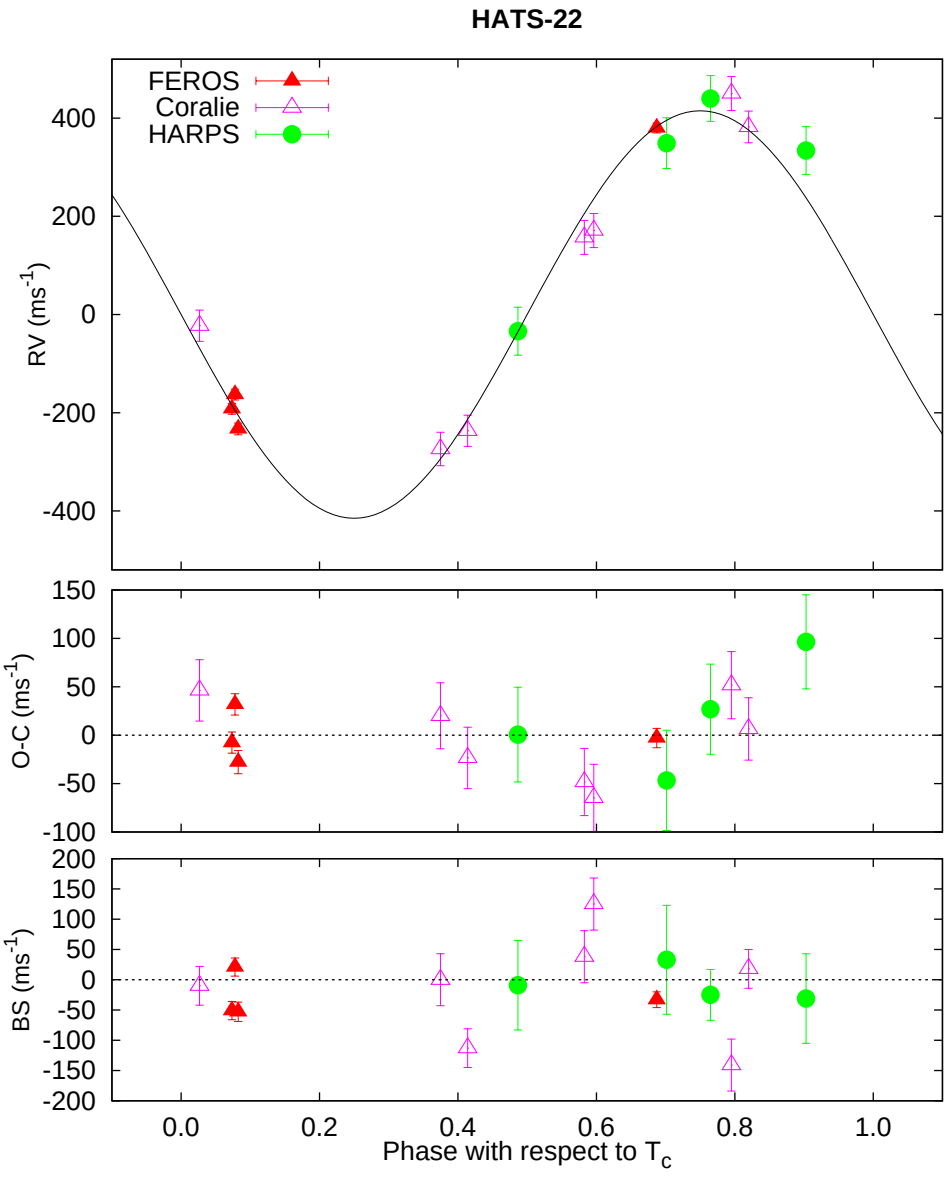
HATS-22
FEROS
Coralie
HARPS
RV (ms-1)
O-C (ms-1)
BS (ms-1)
Phase with respect to Tc

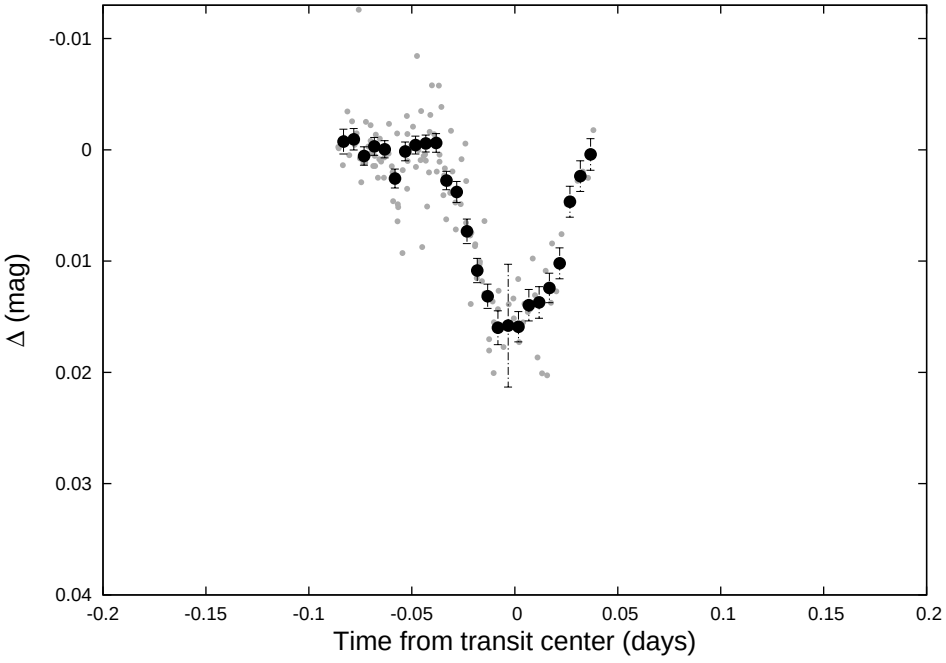
-0.01
0
0.01
0.02
0.03
0.04
Δ (mag)
-0.2
-0.15
-0.1
-0.05
0
0.05
0.1
0.15
0.2
Time from transit center (days)

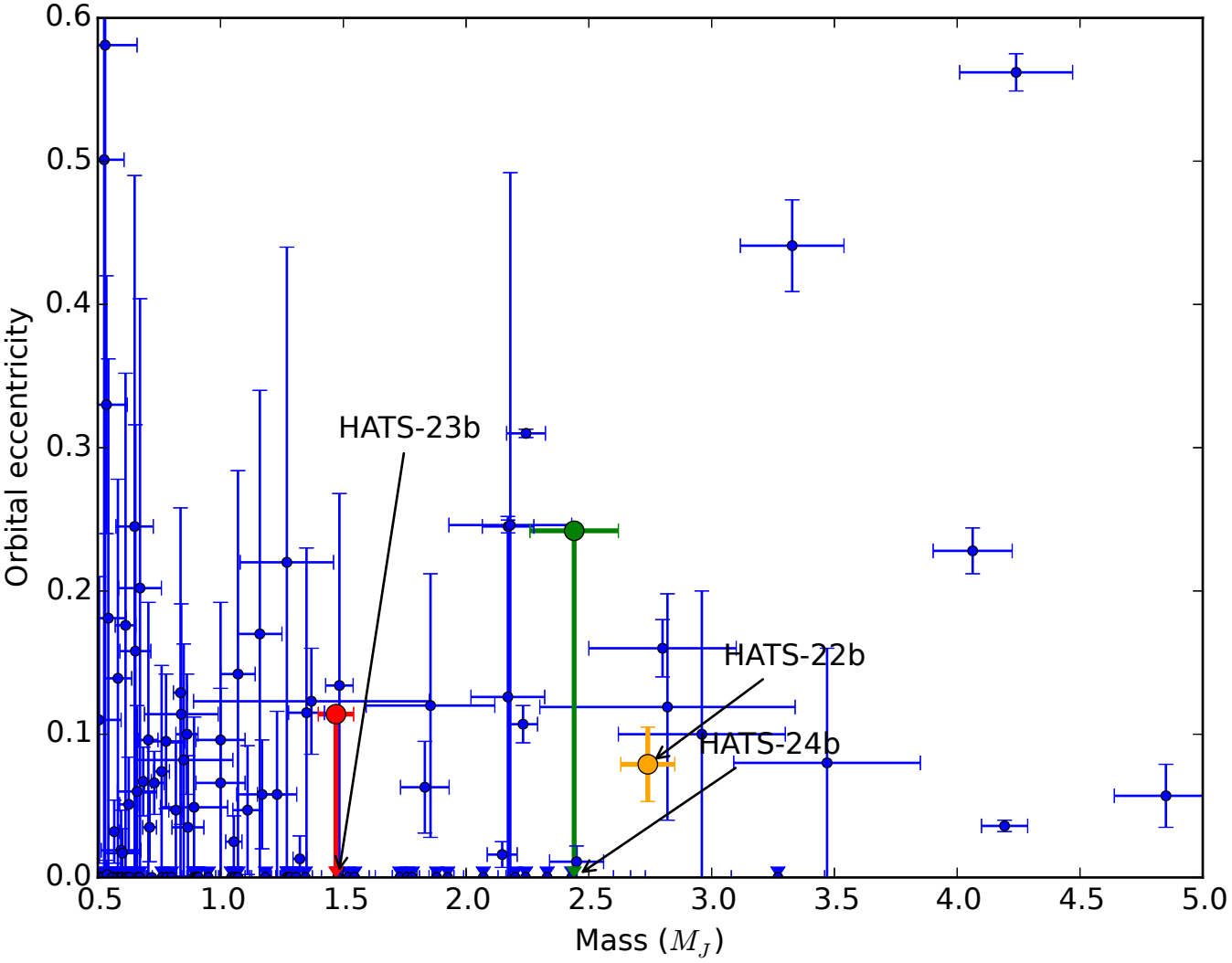
0.6
0.5
0.4
0.3
0.2
0.1
0.0
Orbital eccentricity
HATS-23b
HATS-22b
HATS-24b
0.5
1.0
1.5
2.0
2.5
3.0
3.5
4.0
4.5
5.0
Mass (M_J)